University of Cincinnati

Date: 6/13/2019

I, Kranthi Yellugari, hereby submit this original work as part of the requirements for the degree of Master of Science in Aerospace Engineering.

It is entitled:

Effects of Swirl Number and Central Rod on Flow in Lean Premixed Swirl Combustor

Student's name: **Kranthi Yellugari**

This work and its defense approved by:

Committee chair: Ephraim Gutmark, Ph.D.

Committee member: Prashant Khare, Ph.D.

Committee member: Rodrigo Villalva Gomez, Ph.D.

34242

Effects of Swirl Number and Central Rod on Flow in Lean Premixed Swirl Combustor

A thesis submitted to the

Graduate School

of the University of Cincinnati

in partial fulfillment of the

requirements for the degree of

Master of Science

in Aerospace Engineering

College of Engineering and Applied Science

by

Kranthi Yellugari

B. Tech., Mechanical Engineering

RGUKT, Andhra Pradesh, 2014

University of CINCINNATI

Committee Chair : Dr. Ephraim Gutmark, Ph. D.

Abstract

Gas turbine combustors are used to extract chemical energy from the combustion of fuel in presence of an oxidizer to power turbines. Environmental concerns provide motivation to develop more efficient and less polluting gas turbine engines. To achieve good emission performance, lean burn combustors with low pollutant emissions have been developed. These combustors operate at fuel lean conditions and they can be classified into lean premixed and pre-vaporized (LPP) combustor, where the fuel and oxidizer are premixed and pre-vaporized to form a homogeneous mixture in a dedicated region, premixer, just before the fuel-oxidizer mixture enters the combustion chamber, and lean direct injection (LDI) combustor, where the fuel is directly injected into the flame zone without any premixing with oxidizer [1]. The premixing and pre-vaporizing reduce the residence time, the amount of time the gases are in the combustion chamber. The reduction in residence time reduces the NO_x emissions, as the high NO_x emissions are produced with a long residence time in the combustion chamber.

The flow behavior of non-reacting and reacting flow in a lean premixed swirl combustor, adapted from KAUST experimental rig, has been studied using RANS in the commercial software, Ansys - Fluent. Turbulence is modeled using the two equation realizable $k - \epsilon$ model and the turbulence - chemistry interaction is modeled by a flamelet generated manifold (FGM) technique. At first, non-reacting flow was simulated in lean premixed swirl combustor. These simulation results were compared to the experiments done by Sabatino et al. [2] and LES work of Maestro et al. [3]. This non-reacting flow solution was used as an initial condition to the reacting flow for a faster convergence of the solution, with methane-air mixture at an equivalence ratio of 0.67. GRI 3.0 mechanism was used for modeling chemistry, which had 325

chemical equations and 53 species to solve. The reacting flow results were compared with the experiments of Palies et al. [4]. Analyses are conducted to study the effect of swirl number and a cylindrical rod on the non-reacting and reacting flows.

Higher axial velocities are observed in reacting flow, when compared to the non-reacting flow, because of the thermal expansion of the gases. Flow reattachment point to the combustion chamber wall after the expansion was moved upstream at high swirl numbers. A central toroidal recirculation zone (CTRZ) was observed from a swirl number, S = 0.52 in the case with a central rod, and from S = 0.54 in the case without a central rod and it helped to stabilize the flame. At low swirl numbers, the central rod, which was in the injection tube, helped the flow and flame to stabilize on top of it. In the absence of this central rod, the flame is lifted off and stabilized at a distance from the burner exit. Also, the flame length was shortened at high swirl numbers. As the swirl number was increased, the CTRZ started to move upstream. This phenomenon with flame flashback was observed from S = 0.7. A very high turbulence was observed in the inner shear layer. At high swirl numbers, as the CTRZ moved upstream, the turbulent kinetic energy was very high near the burner exit and the in shear layers. Central rod is best suited at low swirl numbers. Whereas, at high swirl numbers (S>0.6), the need for the central rod is minimized.

NO_x emissions are higher in the regions of high temperature. Along the downstream direction, the NO_x concentration is increased. But, it starts to decrease near the exit of the combustion chamber due to the decrease in the temperature. Due to high temperatures in CTRZ, higher NO_x was observed in CTRZ. The NO_x concentrations decrease with increasing swirl numbers. The case without the central rod produced slightly lower NO_x, when compared to the case with the central rod. This was because of the lower temperatures observed in the case without the central rod.

Acknowledgments

I would like to thank my advisor Dr. Ephraim Gutmark for his support and guidance throughout the program. His technical expertise and insights have helped me to gain good exposure to the field of propulsion. I am so grateful for the time and help that he has put on me.

I am so thankful to Dr. Prashant Khare for his immediate acceptance to be part of the thesis committee, even in his busy schedules.

I would like to thank Dr. Rodrigo Villalva for his continuous help and guidance in building this thesis work.

I specially thank Dr. Urmila Ghia, for supporting me all the time.

I would like to thank Ohio Supercomputer Center for letting me use the resources.

I would like to thank my friends and people from work, for being patient, cooperative and supportive all these years in Cincinnati.

All this could not be possible without my parents and my older brother. I so grateful to my parents and my brother for always believing in me.Their unconditional love and support always made me to dream big and achieve my dreams with ease.

Finally, I am so thankful to my Master and Sir for their continuous blessings and guidance throughout my life .

Contents

List of Figures

List of Tables

Chapter 1

Introduction

Gas turbine combustors are used to extract chemical energy from the combustion of fuel in presence of an oxidizer to power turbines. Environmental concerns provide motivation to develop more efficient and less polluting gas turbine engines. To achieve good emission performance, lean burn combustors with low NOx emissions have been developed. These combustors operate at fuel lean conditions and they can be classified into lean premixed and prevaporized (LPP) combustor, where the fuel and oxidizer are premixed and pre-vaporized to form a homogeneous mixture in a dedicated region, premixer, just before the fuel-oxidizer mixture enters the combustion chamber, and lean direct injection (LDI) combustor, where the fuel is directly injected into the flame zone without any premixing with oxidizer[1]. The pre-mixing and pre-vaporizing reduce the residence time, the amount of time the gases are in the combustion chamber. The reduction in residence time reduces the NO_x emissions, as the high NO_x emissions are produced with a long residence time in the combustion chamber.

1.1 Objectives

The main objectives of the thesis are to study the effects of swirl number,

- In non-reacting and reacting flows
- With and without a cylindrical central in the injection tube

1.2 Motivation

The actual flow and the combustion process may be expensive and difficult to quantify by the experiments. To overcome this issue and to provide in detail explanation of the physics involved, numerical simulations are an effective way understanding the physics. These numerical simulations complement the experiments, and are useful in validating a conceptual design. The research work in this thesis has been motivated by the need to provide a better understanding and quantitative results in a cost effective way. A very limited research has been done on the effects of a central rod at varying swirl intensities. The main motivation is to develop a computationally economical tool to study the flow and combustion dynamics.

1.3 Outline of the Thesis

The contents of this thesis include four chapters following this chapter. Chapter 2 provides the theoretical background for the topics like turbulence and combustion, involved in the current research work. This is followed by the description of the experimental rig , problem statement, numerical methodologies applied to solve the problem in chapter 3. The results that are obtained from the numerical setup, are explained in chapter 4. Chapter 5 is concluded with

the validation of the results and with some major findings. Also, the future scope of the work is discussed in this chapter.

1.4 Literature Review

Turbulence is a challenge in the field of fluid dynamics because of its highly non-linear behavior. Even though the research on turbulence had started more than a century back, researchers are still exploring the new ways of tackling it through experiments and numerical modeling. Turbulence can be modeled using Reynolds Averaged Navier-Stokes (RANS) , Direct Numerical Simulation (DNS), and Large Eddy Simulation (LES). RANS modeling is used for solving the engineering problems, whose complexity is low to moderate. For the problems with high complexity, LES is an effective tool. DNS is an excellent tool for understanding turbulent dynamics and developing turbulence models. But, it involves enormous computational costs and requires a very large memory. A lot of researchers have worked on these models for analyzing the turbulence.

Premixed combustion is much more difficult than non-premixed combustion to model. Because, the flame is thin and stretched in premixed combustion, which makes it difficult to capture through simulations. Computationally, to capture turbulence-chemistry interaction, a correct model has to be chosen to predict the results accurately. A lot of researchers have successfully modeled premixed combustion along with turbulence using different models like finite-rate, eddy-dissipation, eddy break-up, Zimont's, Peter's, eddy-dissipation concept, flamelet generated manifold (FGM). The following sections provide an insight of the literature review of the works done by the researchers.

1.4.1 RANS Models for Turbulence

Guo et al. [15] simulated turbulent swirl flow in an axisymmetric sudden expansion. Turbulence was modeled using standard $k - \epsilon$ model for different swirl numbers. They found that the precessing vortex core is a default characteristic of a swirling flow in a sudden expansion. The results produced by the standard $k - \epsilon$ model were very much in agreement with the results from the experiments. In one of the researches, AbdelGayed et al. [16] worked on the flow characteristics in a lean premixed swirl stabilized combustor. Realizable $k - \epsilon$ and detached eddy simulations(DES) models were used to capture the flow behavior. Realizable $k - \epsilon$ model was able to capture the recirculation zones accurately. But, failed to predict the detailed flow structures like the vortex shedding and precessing vortex core. DES was used successfully to capture the detailed flow characteristics. Baej et al. [17] used shear-stress transport (SST) for modeling turbulence. Different nozzles with different swirl numbers were analyzed. Umeh et al. [18] modeled an axi-symmetric lean premixed combustor to study the phenomena of swirling flows and vortex breakdowns. Realizable $k - \epsilon$ model was used for capturing the turbulence.

1.4.2 Premixed Combustion

Huang et al. [6] focused on the effect of swirl number on the flow and combustion dynamics using LES along with a flamelet library approach to model turbulent premixed combustion. A central toroidal recirculation zone (CTRZ) was observed when the swirl number reached a critical value. Also, flame flashback was observed as the swirl number was increased. Figure 1.1 shows the mean temperature contours for two swirl numbers, S = 0.44, 1.10. Devikanandan [19] worked on a lean premixed combustor to analyze the flow and flame dynam-

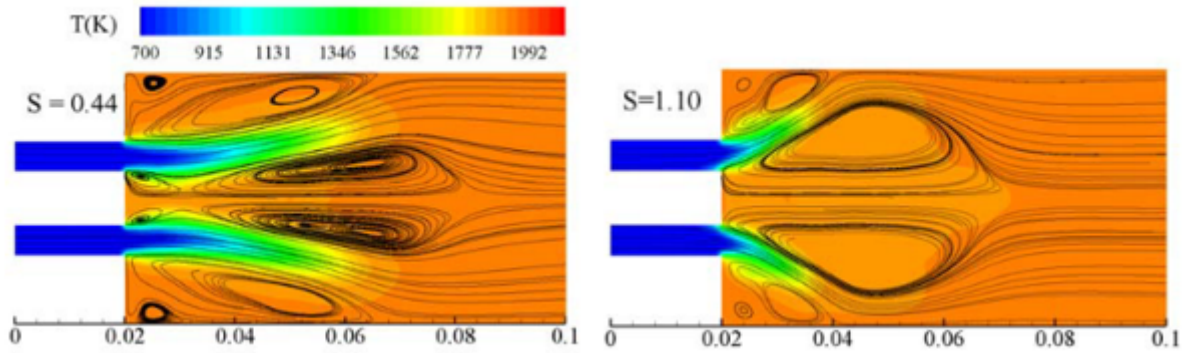

Figure 1.1: Mean temperature contours for swirl numbers, S = 0.44 and 1.10[6]

ics. LES was used to model the turbulence and finite-rate/eddy-dissipation (FR-ED) model was used for the study of turbulence-chemistry interaction. Flame was observed to be stabilized between the vortex structures and experienced shear-layer instabilities. Also observed that eddy structures in the reacting case are much thicker than the non-reacting case. This was because of the viscosity's temperature dependence, which affects the flow stabilization. Mansouri et al [7] studied the effects of swirl number on flow and flame. Figure 1.2 shows the axial velocity contours for different swirl numbers, ranging from 0 to 1.4. As the swirl number was increased, the CTRZ moved upstream. Also, the flame moved upstream of the combustion chamber and length of the flame got shortened with increasing swirl numbers. Figure 1.3 shows the mean temperature contours for different swirl numbers. Abdelgayed et al [20] investigated flame vortex interactions and acoustics in a lean premixed swirl stabilized combustor using the unsteady RANS and modeled the turbulence-chemistry interaction by finite-rate/eddy-dissipation model. They found that the vortex shedding occurred due to the periodic heat release rate, which caused more perturbations at the inlet. Also, there was more vortex shedding, as the shear layer extended further downstream of the combustion chamber. Abou Taouk et al [21] validated an optimized multi-step global reaction mechanism for methane-air combustion flame using the RANS and unsteady RANS in combustor with a circular and square liners. They observed that RANS modeling failed for the square liner. The turbulence model, SAS-SST model, failed to capture the velocity field accurately in the open liner. Anetor et al [22] used reduced

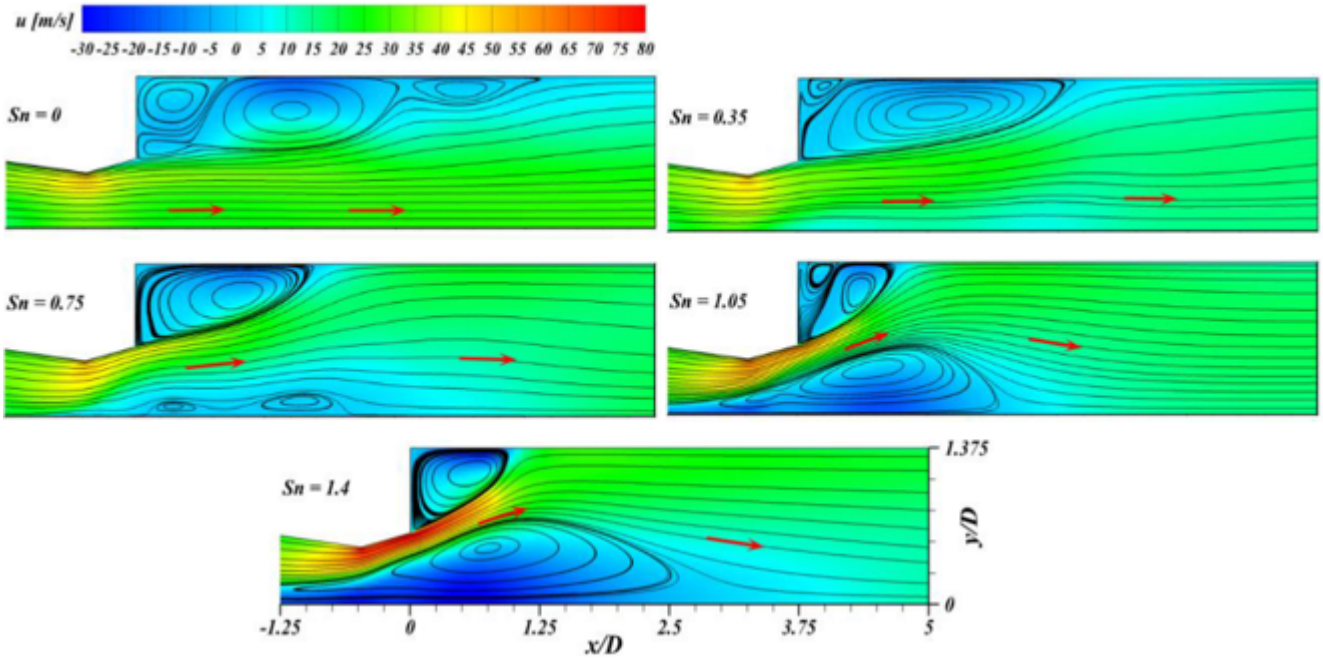

Figure 1.2: Axial velocity contours at different swirl numbers [7]

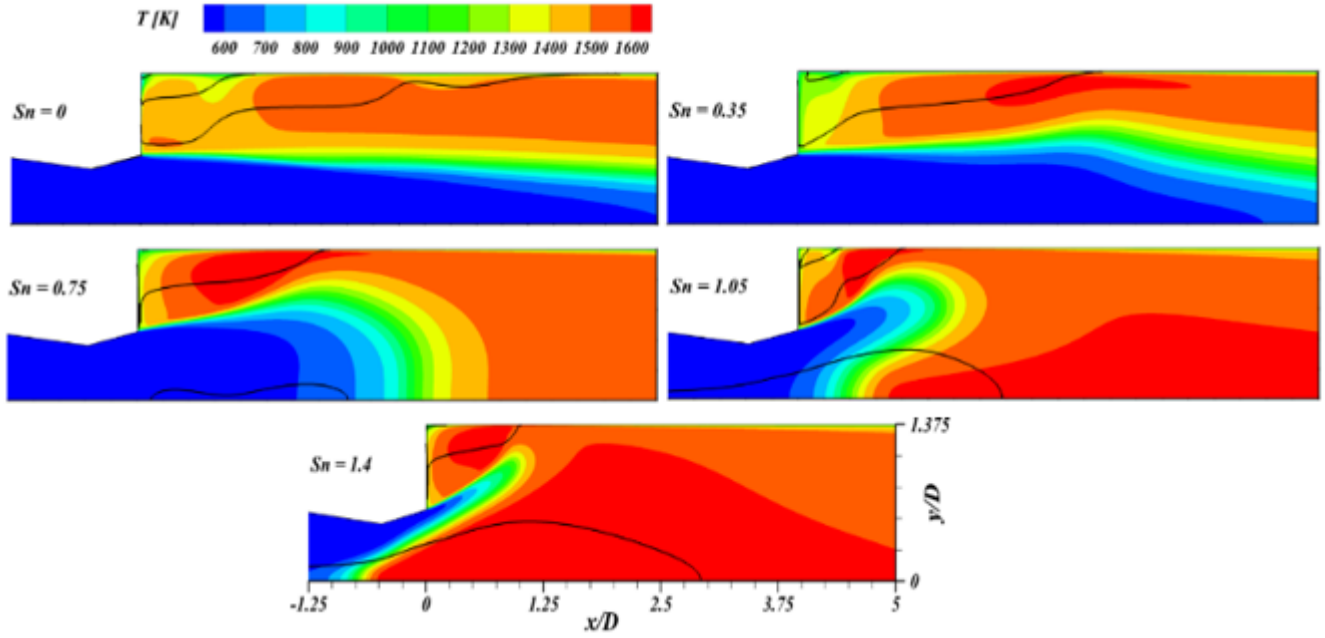

Figure 1.3: Mean temperature contours at different swirl numbers [7]

reaction mechanism instead of a detailed chemistry mechanism to study the premixed combustion product species. They found that the peak flame temperature is under the estimated adiabatic flame temperature of the propane-air mixture by 16%, and the maximum temperature was found in the regions where the swirl intensity is very high. Ouali et al. [8] studied the effects of swirl intensity on the flow field along with the thermal NO_x emissions in a low swirl

intensity burner. Figure 1.4 shows the temperature and thermal NO_x distributions along the centerline for different swirl numbers. The temperature along the centerline decreases with the increase in the swirl number. Also, it was observed that the concentration of NO_x increased with increase in temperature and it decreased with the higher swirl intensities.

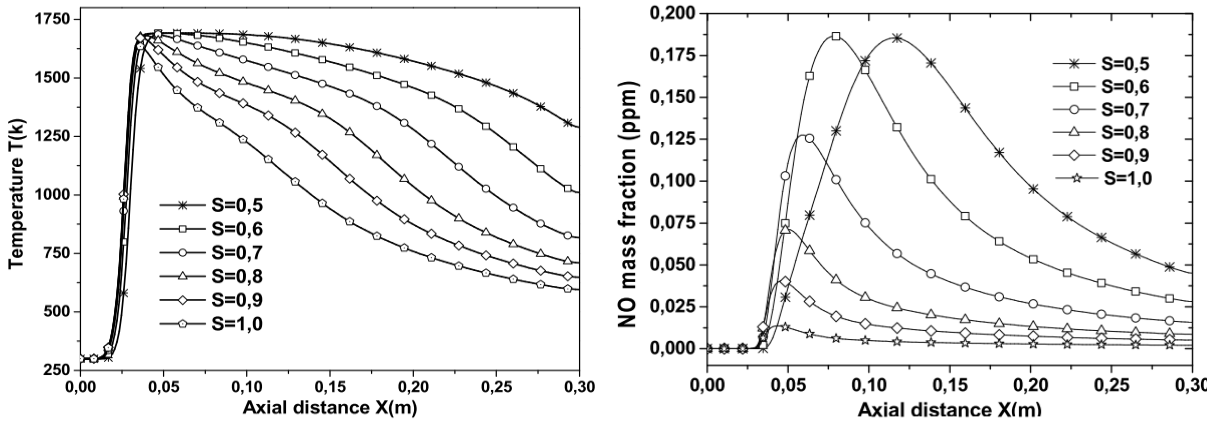

(a) Temperature distribution along the centerline **(b)** NO_x concentration along the centerline

Figure 1.4: Temperature distribution and NO_x concentrations along the centerline for different swirl numbers[8]

Pampaloni et al. [23], used FGM with RANS and LES. RANS-FGM was successful in predicting the flow characteristics in reacting flow along with species concentrations.Veiga [24] worked on a lean premixed hydrogen combustor using RANS modeling for turbulence. Eddy dissipation concept (EDC) and flamelet generated manifold (FGM) models were used to study the turbulence-chemistry interaction. The flow field in the reacting case was not well captured because of the different mixing patterns used the chemistry models. Even the RANS models applied were not satisfactory for hydrogen-air mixing in the combustor. Li et al [25] studied the characteristics of lean premixed swirl stabilized combustor with LES. They observed that the premixed flame regime increased with the increase in the swirl number which in turn increased the shear layer. The vortex breakdown instability increased with the increase in the Reynolds number. Also, they studied the flame lengths and heat release, which got reduced with rise in nitrogen concentration. This increase in the mass of the nitrogen resulted in the

blockage of the swirl flow and there by reducing the size of the recirculation zone.They showed that the conversion of bubble and helix type vortex breakdown are related directly with the swirl number. Bahramian et al [26] simulated a premixed combustor in 2-D and 3-D using EDC and finite-rate/eddy-dissipation model. EDC model predicted an increase in velocity at the nozzle exit and exhaust zones. The recirculation zone shifted downstream of the combustion chamber,where as with the finite-rate/eddy-dissipation model, the recirculation zone stayed at the bottom of the chamber. FR-ED model gave a fast reaction with the simple global mechanism. Maximum temperature at the burner head was higher in EDC model thatn in FR-ED model. Bao [27] compared different turbulence models, all the $k - \epsilon$ models and the Reynolds stress model (RSM). The RSM model predicted the peak temperature better than the other models. A new EDC model was proposed to study the turbulence-chemistry interaction. It performed better than the existing models. The NOx concentrations were greatly reduced.

Oijen et al [28] developed a new model, the flamelet generated manifold (FGM) model, to study the premixed laminar combustion. This model reduced the computational time to a great extent. The flame front along with the mass fractions were predicted very well. Ouali et al [29] used a presumed β probability density function (PDF) to study the premixed combustion. They studied the swirl and equivalence ratio effects on the flame and the emissions. Increase in the equivalence ratio did not affect the NOx emissions. The flame front was most significant in radial boundaries where the temperature was important. Also, they had the flame detached from the nozzle exit. Ramaekers et al [30] applied FGM model to analyze the turbulent partially premixed flames. This model did not perform well in non-premixed regions. There was no interaction between the flamelets. They observed that increasing the turbulent intensity gave good results for the turbulent flame models. Kedukodi et al [31] modeled a premixed combustor for studying the heat transfer in premixed combustion. FGM model was used

to simulate the reacting flow in the combustion chamber. The swirling jet impinges far downstream in terms of a reacting flow than a non-reacting flow, because of the high heat release and the damping of the vortex in the hot flow. The length of the central vortex got reduced in the reacting flow in comparison to the non-reacting flow. There was an increase in the turbulent kinetic energy with the increased swirl angle. Nakod et al [32] accurately predicted the flame lift off in methane-air premixed combustion. The simulations were performed using the FGM and laminar flamelet models. The computational time for the FGM model was $0-10\%$ greater than the laminar flamelet model, depending on the type of flame.

Shelil et al [33] modeled premixed combustion with $85\%CH_4$ and $15\%CO_2$ using the turbulent flame speed model. They observed that there was a flashback not because of the reversed flow. They found that the flashback occurs as a function of mass flow rate and indirectly the velocity and the equivalence ratio. They analyzed that a better resistance was offered to the flashback at fuel lean conditions when the turbulent flame speed was lowered. Also, they observed that, in flashback the recirculation zone was wider and the velocity was greater than the velocity in normal combustion. Tidswell et al [34] validated the available turbulent flame speed models applied to hydrogen/methane/air combustion. They worked on Zimont's model, Peter's model and enhanced coherent flamelet model (ECFM). Zimont predicted hydrogen enrichment partially increased reaction intensity, and the axial velocity in the flame region was not predicted well. Peter's model predicted flashback at 100% hydrogen enrichment. The initial predictions were poor with ECFM. All the models performed well only till 60% of hydrogen enrichment. So, they proposed a modified Zimont model, which got very good results at 100% hydrogen. Hipp [35] studied 2-D lean premixed methane-air combustion in turbulent flame speed combustion model (TFCM) and EDC model. The EDC model did not predict the flame shape and position accurately, where as TFCM correctly predicted the shape and

position. Polifke et al [36] did research on inhomogeneously premixed combustion using an extended version of TFCM. This extended version performed better than the finite rate model.

1.4.3 Premixed Combustion in Experiments

Experiments are the most practical means of analyzing combustion. Palies et al. [4] studied the effects of swirl on the flow using a radial swirler. Two swirl numbers, S = 0.55 and 0.65 were considered for the study. Figure 1.5 shows the velocity profiles for these swirl numbers. As the swirl number was increased, there was an increase in the azimuthal velocity. Axial velocity was also increased. But, when compared to the azimuthal, the increase was very small.

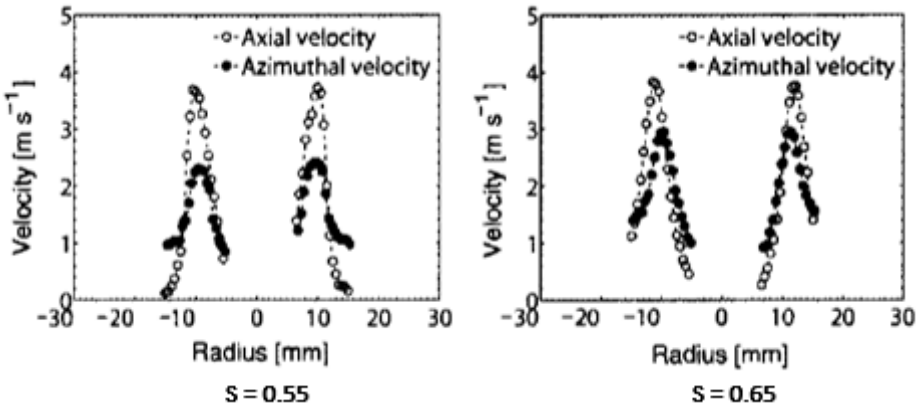

Figure 1.5: Mean velocity profiles for swirl numbers, S = 0.55 and 0.65 [4]

In an another study, Durox et al. [9] experimented with a variable blade swirler. Different blade angles were analyzed ranging from 23° to 61°. CTRZ started to form from 38°. Figure 1.6 shows the velocity profiles for different blade angles and it is observed that the CTRZ increases with an increase in the blade angle.

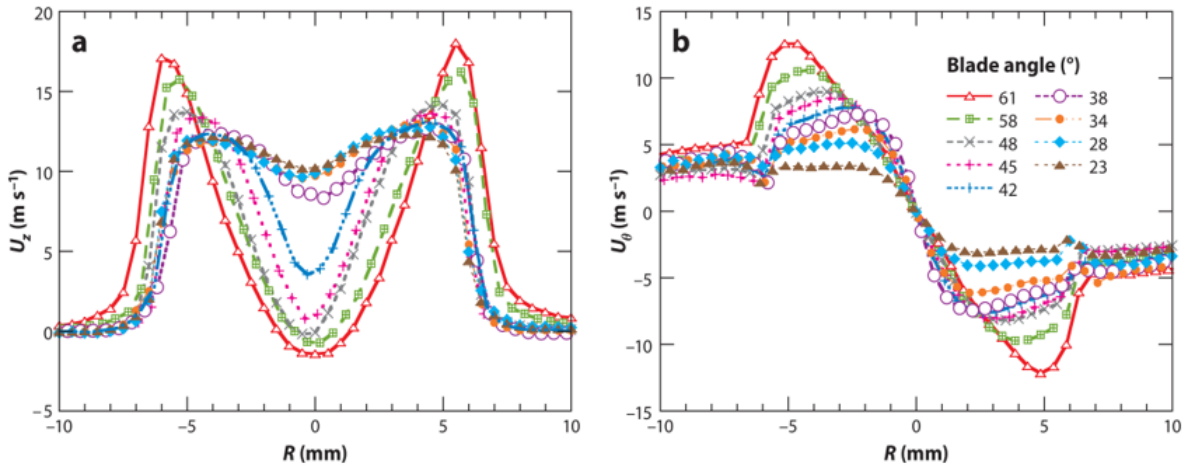

Figure 1.6: Mean velocity profiles for swirl numbers, S = 0.55 and 0.65 [9]

Park et al. [37] studied effects of reaction on the flow in lean premixed swirl stabilzied combustor. Some significant changes were observed in presence of a reaction on the flow. Figure 1.7 shows the mean TKE contours in non-reacting flow, on the left, and reacting flow, on the right. It was observed that turbulence was high in inner shear layers for the reacting flow, and it was near the burner exit for the non-reacting flow.

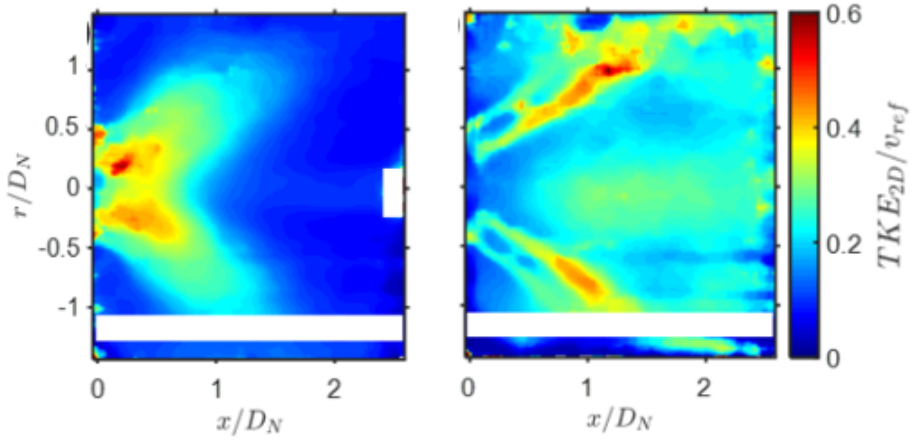

Figure 1.7: Mean turbulent kinetic energy contours in non-reacting and reacting flows (White color represents regions where noise covers the signals)

In one of the studies, Elkady et al. [10] used detailed chemistry to predict NO_x and CO emissions in a premixed environment. Figure 1.8 presents the thermal NO_x variation with the adiabatic flame temperature. NO_x showed strong affinity to increasing flame temperature.

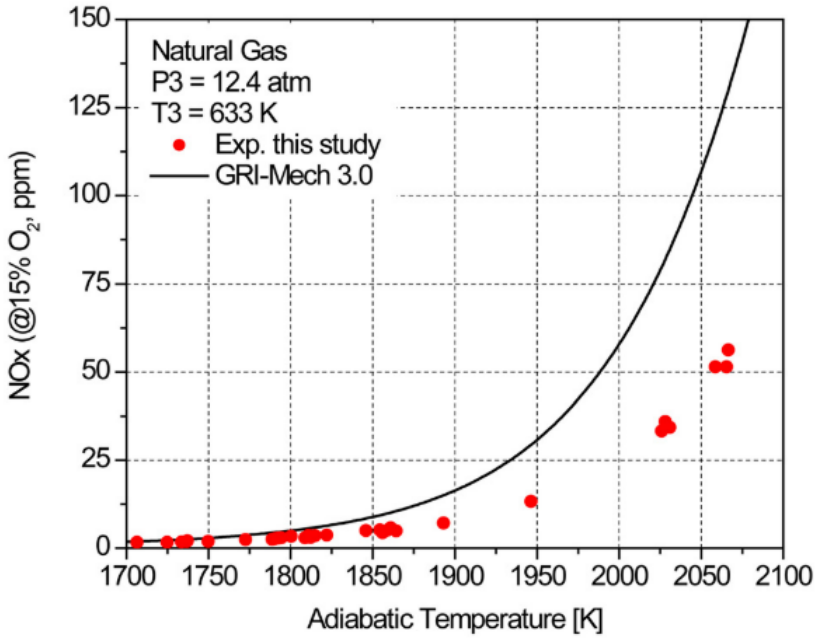

Figure 1.8: NO_x variation with adiabatic flame temperature[10]

Takagi et al. [11] experimented the characteristics of combustion and formation of pollutants in the two types of swirling flames, lean and rich. Fuel lean flames produced lower NO_x than the fuel rich flames. Radial distribution of NO_x concentrations were presented in figure 1.9. The concentration of NO_x increased in the downstream direction. But, it decreased in regions of low temperature near the exit of the chamber.

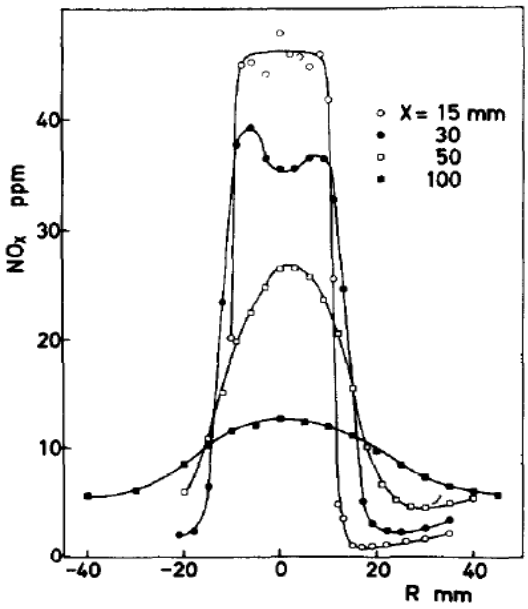

Figure 1.9: Radial distribution of NO_x in the downstream direction of the combustion chamber[11]

Chapter 2

Theory

This chapter covers the basic theories related to the current research work, which involves turbulence and combustion modeling

2.1 Swirl Flow Characterization

Swirling flows are a result of a spiral motion imparted to the flows. A swirl velocity component is applied to generate the spiral motion. This can be achieved by making the flow to pass through swirl vanes or by directly making the flow to enter the chamber tangentially or by swirl generators, where the flow is fed axially and tangentially into the chamber. Swirl has a larger impact on the flow fields like the jet spread and growth in the cold or non-reacting flows, size, shape and stability of a flame and intensity of combustion in reacting flows. The degree of a swirl is characterized by a dimensionless number, swirl number, denoted by **S** [12]. It is defined as the ratio of axial flux of swirl/tangential momentum to the radius times the axial flux

of axial momentum and is given as:

$$S = \frac{R\int_0^R \rho u v 2\pi r^2 dr}{R\int_0^R \rho u^2 2\pi r dr} \tag{2.1}$$

where ρ is the density of the fluid, u is the axial velocity, v is the tangential velocity, r is the radius and R is the characteristic radius.

In the above expression, the pressure term in the axial momentum flux is neglected. If the swirl number, $S \leq 0.4$, the swirl is considered as low swirl. The effect of this low swirl is to increase the width of a jet flow and it increases with increase in the swirl number as shown in figure 2.1a. There might be significant pressure gradients at any axial location from an approximate pressure distribution as a result of the swirl motion. The pressure gradient is given as:

$$\frac{\partial p}{\partial r} = \frac{\rho w^2}{r} \tag{2.2}$$

The above equation is a reduced form of the radial momentum equation with all the turbulence terms neglected. For a very low swirl, i.e., $S \leq 0.2$, the pressure gradients may be neglected from the analyses. When the swirl number is larger than 0.5, the swirl is considered to be a stronger swirl. At these stronger swirls, there will be strong radial and axial pressure gradients at the exit of the nozzle, creating a axial recirculation region, called the central toroidal recirculation zone (CTRZ) as shown in figure 2.1b. This is because of the centrifugal effects generated by the large radial pressure gradients. Turbulent intensity will be maximum in these recirculation regions. On the boundaries of the reverse flow, the mean velocity is zero and the local turbulence intensity reaches to infinity. The size and shape of the recirculation zone and the regions of high turbulence intensity, always important to the stability of the flame and combustion performance. Irrespective of the type of swirl generator used, the center/the eye of the

recirculation zone always develops close to the nozzle exit. Development of recirculation zone is always a rare phenomenon in case of low swirl flows.

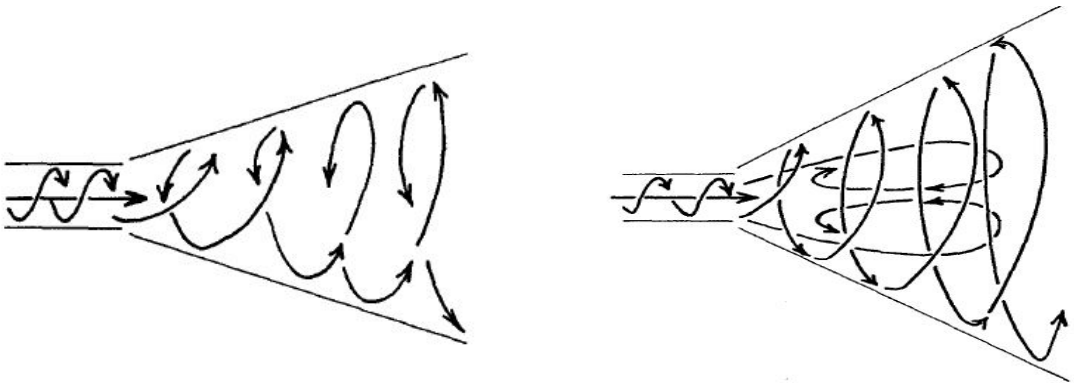

(a) Low swirl, $S \leq 0.4$ **(b)** High swirl, $S \geq 0.5$

Figure 2.1: Swirling jet flows with low and high swirl numbers [12]

2.1.1 Vortex Breakdown

Vortex breakdown refers to a sudden change in the structure of the flow when the swirl level is greater than the critical value. It is characterized by deceleration in the flow direction, developing a stagnation point, beyond which the flow is separated with turbulence behind it. Increase in the swirl develops a strong coupling between the tangential and axial velocity components. When this coupling reaches a point where the kinetic energy of the flow cannot overcome the adverse pressure gradient along the axis of the jet, a recirculation zone-a form of vortex breakdown, is developed in the central region of the jet [38]. A lot of researchers have worked on observing this flow phenomenon. Leibovich [39] described the vortex breakdown phenomenon as a change in the vortex structure developed by the change in the tangential and axial velocity components. Sarpkaya [13] and Harvey [40] showed that the vortex breakdown takes the form an axisymmetric bubble of recirculation fluid. Faler and Leibovich [41] described vortex breakdown in six forms depending on the Reynolds number. All these forms were considered either as a bubble form or spiral form. Figure 2.2 shows a near

axisymmetric vortex breakdown from one of the experiments of Sarpkaya [13].

Figure 2.2: Near axisymmetric vortex breakdown [13]

2.1.2 Flame Stabilization by Swirling Flows

Most of the modern combustors and gas turbine engines achieve flame stabilization by a swirling flow or a vortex breakdown phenomenon. In the jet flows with high tangential/swirl velocities, if the swirl number exceeds a critical value, a vortex type recirculation region is created in the central region of the jets near the nozzle exit. This recirculation region plays a crucial role in the flame stabilization as it has well mixed hot combustion products which act as a heat source. These hot gases transfer the heat and mass to the fresh incoming reactants by courtesy of the high turbulence in the recirculation region. This continuous provision of heat to the reactants stabilizes the flame from extinction. These recirculation regions have similarities with those produced by bluff bodies. The length of the flame and the distance from the burner, where the flame is stabilized are considerably shortened [12].

2.2 Lean Premixed Combustion

The effectiveness of combustion is governed mainly by the concentrations of fuel, air and lot of other factors. There are various methods to distribute fuel- oxidizer mixture

required for the combustion to the flame. One among them is the premixed combustion. In the premixed combustion, the fuel and the oxidizer are mixed homogeneously before they enter the combustion chamber, to form a homogeneous mixture and to reduce the residence time. The equivalence ratio in the premixed combustion can be controlled. This offers a means to attain low temperatures, which reduces the production of NOx emissions. These NOx emissions are major pollutants. Especially, when the premixed combustion is occurring at lean burning condition, i. e., the equivalence ratio $\phi < 1$. The advantages of operating at lean mixture conditions are high thermal efficiency and avoids local hot spots which are high temperature regions [42].

In the lean premixed (LPM) combustion systems, nitrogen in the combustion air acts as a diluent, as fuel is mixed with air upstream of the combustor at fuel-lean conditions. The fuel-air ratio approaches one-half of the ideal stoichiometric level, resulting in excess air to burn the fuel. This excess air is a key to limit NOx formation, because the lean conditions cannot produce the high temperatures that create thermal NOx. Gas turbine engine is one of the major applications of the LPM combustion. Most of the LPM gas turbine engines utilize swirling flows to stabilize the flame for clean and complete combustion. One of the most important flow features generated by the swirler is a central toroidal recirculation zone (CTRZ), which helps to stabilize the flame. Flows in this region are associated with high shear rates and strong turbulent intensities resulting from vortex breakdown.

Even though the premixed combustion has a major disadvantage in terms of flash-back, where the flame travels upstream and damages the system, it can be more efficient than the diffusion/non-premixed combustion. The flame velocity varies with the thermal diffusion a, $S_l = a/t_c$. The premixed combustion does not depend directly on the species mixing, as they are premixed. The flame velocity can be increased with the thermal diffusion, a, by increas-

ing the unburnt temperature. This helps to control the flame speed easier than the diffusion flames. The flame temperature can be controlled by the stoichiometric ratio of the mixture. As mentioned earlier, this controls the production of NOx. But, the maximum diffusion flame temperature cannot be controlled as the mixture is not controlled. This is the main reason to consider and use premixed combustion with the drawbacks being better controlled.

2.2.1 Dimensionless Numbers [5]

Turbulent Reynolds number

The Reynolds number Re, evaluates the inertial force relative to the viscous force. Similarly, a turbulent Reynolds number Re_t is defined using the turbulent scales:

$$Re_t = \frac{u' l_t}{\nu} \tag{2.3}$$

where u' is the velocity fluctuation, l_t is the turbulent length scale, and ν is the kinematic viscosity.

The turbulent Reynolds number can be locally defined as the length scale and the velocity fluctuations, vary with the locations. But, the Reynolds number is defined on a global scale and value is relevant for the whole geometry.

Damköhler number

Damköhler number is based on time scales and it is used to compare the turbulent and chemical time scales. It is given as:

$$Da = \frac{t_t}{t_c} \tag{2.4}$$

where the turbulent time scale is evaluated from the ratio of integral length and velocity scales:

$$t_t \sim \frac{l_t}{u'} \tag{2.5}$$

and the chemical time scale is evaluated from the laminar heat diffusion and the laminar flame speed:

$$t_c \sim \frac{a}{S_l^2} \tag{2.6}$$

If the Damköhler number, $Da < 1$, the chemistry will be slow. Because, the turbulent time scale is smaller than the chemical time scale, so, the turbulence is faster than the combustion. If, $Da > 1$, the chemistry will be very faster.

Turbulent Karlovitz number

Turbulent Karlovitz number compares the chemical time scale to the smallest turbulent scales, Kolmogorov scales. It indicates whether the smallest eddies have any influence on the flame and it is given as:

$$Ka_t = \frac{t_c}{t_\eta} = \frac{\delta_l^2}{\eta^2} = \frac{u(\eta)^2}{S_l^2} \tag{2.7}$$

where δ_l is the relative thickness of the laminar flame front. A second turbulent Karlovitz number is based on the reacting layer on the flame front and indicates whether the smallest eddies are small enough to enter the reacting layer. It is defined as:

$$Ka_\delta \equiv \frac{\delta_r^2}{\eta^2} v = \delta^2 Ka_t \tag{2.8}$$

where $\delta = Ze^{-1}$ defines the relative thickness of the reacting layer δ_r. Ze is the Zeldovich number, δ_l/δ_r, η is defined as $\left(\frac{\nu^3}{\epsilon}\right)^{1/4}$.

The turbulent Reynolds number, Damköhler number and turbulent Karlovitz number can be related using Prandtl number, $Pr = \frac{\nu}{a}$, which estimates the relative diffusion transfer for momentum and heat. The relation is given as:

$$PrRe_t \sim Da^2 Ka_t^2 \tag{2.9}$$

The dimensionless ratios can be written in terms of dimensionless numbers. In combustion regime diagrams, the ratio of u' to the laminar flame speed S_l is largely used. The ratio is defined as:

$$\frac{u'}{S_l} \sim \sqrt{\frac{PrRe_t}{Da}} \tag{2.10}$$

Also, the ratio of the integral length scale, l_t and the flame thickness, δ_l is expressed as:

$$\frac{l_t}{\delta_l} \sim \sqrt{PrRe_t Da} \tag{2.11}$$

2.2.2 Combustion Regimes

There are different regimes of premixed turbulent combustion, based on the chemical and the turbulent scales.

Laminar flames

Laminar flame regime is defined for small turbulent Reynolds number, if $Re_t < 1$

Well stirred reactor

In this regime, the Damköhler number is reduced with a moderate turbulence intensity. This regime is defined if, $Da < 1$ and $Ka_\delta < 1$. In this regime, the turbulent time scale is smaller than the chemical scale. But, the smallest eddies are not fast enough to enter and disrupt the flame front's inner layer. Turbulence can make the mixture homogeneous, before the combustion takes place. So, the chemical mechanism is dominant than the turbulence.

Wrinkled and corrugated flame regime

These two regimes are defined for large Damköhler numbers with a moderate turbulence intensity. These are bounded from each other by the relative flame speed. The two regimes are defined as:

$$wrinkled flame : Da > 1, Re_t > 1, Ka_t < 1 \; and \; \frac{u'}{S_l} < 1 \tag{2.12}$$

$$corrugated flame : Da > 1, Re_t > 1, Ka_t < 1 \; and \; \frac{u'}{S_l} > 1 \tag{2.13}$$

If the flame is place in a weakly turbulent flow, then the regime corresponds to wrin-

kled flame. If the flame front is more folded due to the larger turbulent velocity, then the regime is called the corrugated flame regime. For both the regimes, the flame front is considered as a collection of flamelets. Each flamelet in the flame front behaves as a laminar flame. They behave differently because of the local action of the eddies. These eddies cannot enter the flame front and modify the flame front's structures.

Thickened flame regime

In this regime, the smallest eddies can enter the flame front or the preheated zone. Re_t and Ka_t are larger in the regime. The regime is defined as:

$$Da > 1, Re_t \gg 1, and\ Ka_t > 1 \tag{2.14}$$

The smallest/Kolmogorov eddies increase the diffusion in the flame front, so the thickness of the flame front increases. This results in a thickened flame.The flamelet velocity of the thickened flame will no longer be identical to laminar flame speed. The chemical and turbulent scales are dependent on each other.

Broken zone regime

This regime develops when the turbulence intensity is more intensive than the thickened flame regime. The smallest eddies enter the flame front and even the reactive layer, δ_r, as they are very small. The regime is defined as:

$$Da > 1, Re_t \gg 1\ and\ Ka_\delta > 1 \tag{2.15}$$

Since, the eddies enter the inner layer zone, the reactive layer, the flamelet velocity is reduced and may result in local extinction of the flame. This phenomenon is called quenching. The limit between the thickened and the broken flame regime is hard to define. As it is dependent on various factors like chemical properties of the mixture, instantaneous and local turbulence conditions.

2.2.3 Turbulent Premixed Combustion Diagram

A modified Borghi-Peters diagram is used to depict all the combustion regimes in one diagram. Borghi was the first to present turbulent regime diagram with the axes u'/S_l and l_t/δ_l. Later, a number of researchers came up with similar diagrams with extended zone separations. The five dimensionless numbers, Re_t, Da, Ka_t, Pr and Ze are used to construct the combustion diagrams. Prandtl and Zeldovich numbers are imposed for specific combustible mixtures. A change in the Zeldovich number will rotate the line, $Ka_\delta = 1$, and change the width of the thickened flame regime. A change in the Prandtl number will scale the complete combustion diagram. The following figure shows the different combustion regimes.

2.3 Governing Equations

The flow is governed by 3-dimensional, both steady and unsteady Navier-Stokes (N-S), while the combustion is governed by species transport equation. The following sections will describe the theoretical formulation of these governing equations, along with turbulence and combustion modeling.

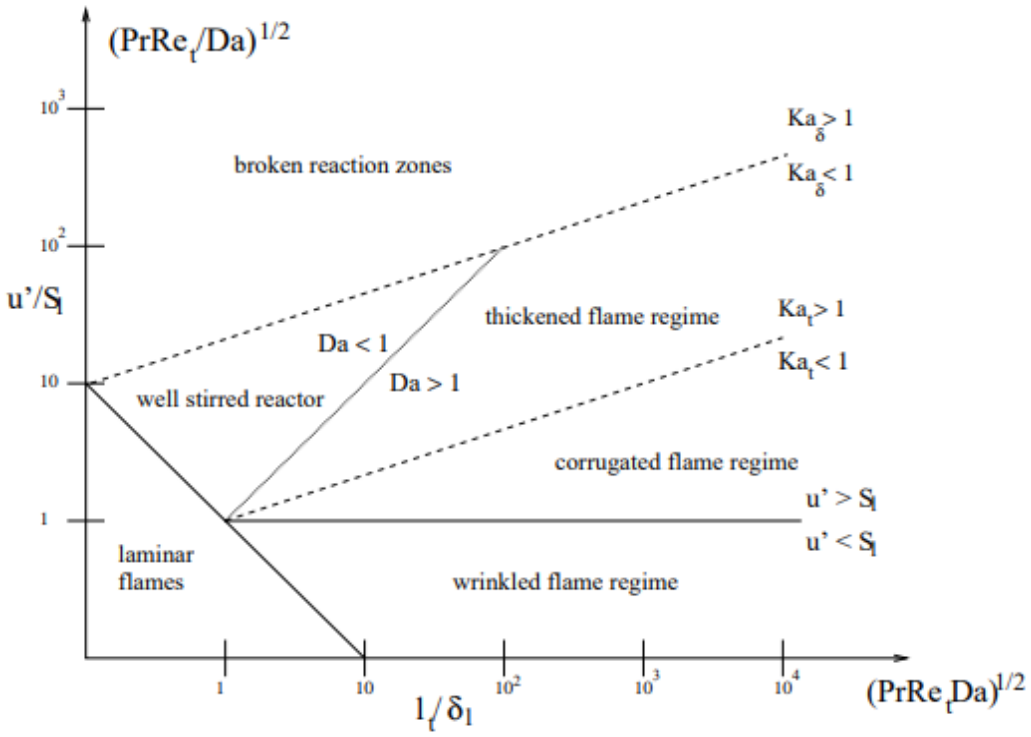

Figure 2.3: Modified Borghi-Peters Combustion Diagram [5]

2.3.1 Navier-Stokes Equations

The 3-dimensional, unsteady form of the Navier-Stokes equations deals with the velocity, pressure, temperature, and density of a fluid in motion,along with their relations. The equations were derived independently by G.G. Stokes, in England, and M. Navier, in France, in the early 1800s. These equations are extensions to the Euler equations and include the effects of viscosity.

The Navier-Stokes equations are a set of coupled differential equations. They consist of a time-dependent continuity equation for conservation of mass, three time-dependent equations for conservation of momentum and a time-dependent conservation of energy equation. There are four independent variables, x, y, z spatial coordinates, and time, t. There are six dependent variables, the pressure p, density ρ, temperature T in the total energy, E_T, and the three components of velocity vector, u, in x, y, z directions, u, v, w respectively. Since, all the dependent variables are functions of all the independent variables. So, the differential equations

are partial differential equations and not ordinary differential equations. The following are the Navier-Stokes equations:

Continuity:

$$\frac{\partial \rho}{\partial t} + \frac{\partial (\rho u)}{\partial x} + \frac{\partial (\rho v)}{\partial y} + \frac{\partial (\rho w)}{\partial z} = 0 \tag{2.16}$$

x-Momentum:

$$\frac{\partial (\rho u)}{\partial t} + \frac{\partial (\rho u^2)}{\partial x} + \frac{\partial (\rho uv)}{\partial y} + \frac{\partial (\rho uw)}{\partial z} = -\frac{\partial p}{\partial x} + \frac{1}{Re}\left[\frac{\partial \tau_{xx}}{\partial x} + \frac{\partial \tau_{xy}}{\partial y} + \frac{\partial \tau_{xz}}{\partial z}\right] \tag{2.17}$$

y-Momentum:

$$\frac{\partial (\rho v)}{\partial t} + \frac{\partial (\rho uv)}{\partial x} + \frac{\partial (\rho v^2)}{\partial y} + \frac{\partial (\rho vw)}{\partial z} = -\frac{\partial p}{\partial y} + \frac{1}{Re}\left[\frac{\partial \tau_{xy}}{\partial x} + \frac{\partial \tau_{yy}}{\partial y} + \frac{\partial \tau_{yz}}{\partial z}\right] \tag{2.18}$$

z-Momentum:

$$\frac{\partial (\rho w)}{\partial t} + \frac{\partial (\rho uw)}{\partial x} + \frac{\partial (\rho vw)}{\partial y} + \frac{\partial (\rho w^2)}{\partial z} = -\frac{\partial p}{\partial z} + \frac{1}{Re}\left[\frac{\partial \tau_{xz}}{\partial x} + \frac{\partial \tau_{yz}}{\partial y} + \frac{\partial \tau_{zz}}{\partial z}\right] \tag{2.19}$$

Energy:

$$\begin{aligned}\frac{\partial (E_T)}{\partial t} + \frac{\partial (uE_T)}{\partial x} + \frac{\partial (vE_T)}{\partial y} + \frac{\partial (wE_T)}{\partial z} = &-\frac{\partial up}{\partial x} - \frac{\partial vp}{\partial y} - \frac{\partial wp}{\partial z} + \frac{1}{RePr}\left[\frac{\partial q_x}{\partial x} + \frac{\partial q_y}{\partial y} + \frac{\partial q_z}{\partial z}\right] \\ &+ \frac{1}{Re}\left[\frac{\partial}{\partial x}\left(u\tau_{xx} + v\tau_{xy} + w\tau_{xz}\right) + \frac{\partial}{\partial y}\left(u\tau_{xy} + v\tau_{yy} + w\tau_{zy}\right) + \frac{\partial}{\partial z}\left(u\tau_{xz} + v\tau_{yz} + w\tau_{zz}\right)\right]\end{aligned} \tag{2.20}$$

where Re is the Reynolds number, the variables q are the heat flux components, Pr is the Prandtl number, the τ variables are the components of stress tensor. A tensor is a result of the product of

two vectors. Velocity vector has three components and the stress tensor has nine components. Each component of the stress tensor is itself a second derivative of the velocity components.

The terms on the left hand side of the momentum equations are the convection terms, whereas the terms on the right hand side of the momentum equations that are multiplied by the inverse of the Reynolds number are called the diffusion terms. The Euler equations does not have any diffusion terms. Since the diffusion terms deal with the boundary layers, therefore, Euler equations cannot model boundary layers.

As the Navier-Stokes equations are coupled system of equations, all the five equations need to be solved simultaneously in order to solve a flow problem. To determine the six unknowns, six equations are required. But, there are only five equations. The sixth equation is the equation of state, which relates the pressure, temperature and density of the gas.
The components of shear stress in the Navier-Stokes equations are given as:

$$\tau_{xx} = \frac{2}{3}\frac{\mu}{Re}\left(2\frac{\partial u}{\partial x} - \frac{\partial v}{\partial y} - \frac{\partial w}{\partial z}\right) \tag{2.21}$$

$$\tau_{yy} = \frac{2}{3}\frac{\mu}{Re}\left(2\frac{\partial v}{\partial y} - \frac{\partial u}{\partial x} - \frac{\partial w}{\partial z}\right) \tag{2.22}$$

$$\tau_{zz} = \frac{2}{3}\frac{\mu}{Re}\left(2\frac{\partial w}{\partial z} - \frac{\partial u}{\partial x} - \frac{\partial v}{\partial y}\right) \tag{2.23}$$

$$\tau_{xy} = \frac{\mu}{Re}\left(\frac{\partial u}{\partial y} + \frac{\partial v}{\partial x}\right) \tag{2.24}$$

$$\tau_{xz} = \frac{\mu}{Re}\left(\frac{\partial u}{\partial z} + \frac{\partial w}{\partial x}\right) \tag{2.25}$$

$$\tau_{yz} = \frac{\mu}{Re}\left(\frac{\partial v}{\partial z} + \frac{\partial w}{\partial y}\right) \tag{2.26}$$

The heat flux terms in the energy equation are expressed as:

$$q_x = \frac{\mu}{(\gamma - 1)M_{ref}^2 RePr}\left(\frac{\partial T}{\partial x}\right) \tag{2.27}$$

$$q_y = \frac{\mu}{(\gamma - 1)M_{ref}^2 RePr}\left(\frac{\partial T}{\partial y}\right) \tag{2.28}$$

$$q_z = \frac{\mu}{(\gamma - 1)M_{ref}^2 RePr}\left(\frac{\partial T}{\partial z}\right) \tag{2.29}$$

Assuming a perfect gas, the equation of state is given by:

$$p = (\gamma - 1)\rho e \tag{2.30}$$

where e is the internal energy. Using the Mach number, temperature can computed from:

$$T = \frac{\gamma M^2 p}{\rho} \tag{2.31}$$

The molecular/dynamic viscosity is computed by Sutherland's law given as:

$$\mu = \frac{1 + \bar{T}}{T + \bar{T}} T^{3/2} \tag{2.32}$$

where $\bar{T}$ is Sutherland's constant, and is equal to $\frac{110^0 K}{T_{ref}}$

The Reynolds number and the Mach number are defined as:

$$Re = \frac{U_{ref} L_{ref} \rho_{ref}}{\mu_{ref}} \tag{2.33}$$

$$M = \frac{U_{ref}}{\sqrt{\gamma R T_{ref}}} \tag{2.34}$$

The following non-dimensional variables are used in the governing equations are written in non-dimensional forms as follows:

$$\begin{gathered} x = \frac{x^*}{L_{ref}} \qquad y = \frac{y^*}{L_{ref}} \qquad z = \frac{z^*}{L_{ref}} \\ u = \frac{u^*}{U_{ref}} \qquad v = \frac{v^*}{U_{ref}} \qquad w = \frac{w^*}{U_{ref}} \\ \rho = \frac{\rho^*}{\rho_{ref}} \qquad p = \frac{p^*}{\rho_{ref} U_{ref}^2} \qquad T = \frac{T^*}{T_{ref}} \qquad t = \frac{t^* U_{ref}}{L_{ref}} \end{gathered} \tag{2.35}$$

where ρ_{ref}, U_{ref}, L_{ref} and T_{ref} are the reference quantities for the respective variables.

2.3.2 Reynolds Averaged Navier-Stokes Equations

The constitutive equations used in the Reynolds averaged Navier-Stokes (RANS) are referred as turbulence models. Although a large number of studies have been performed on the development of turbulence models, there has not been a universal turbulence model that is applicable to all the turbulent flows [43]. Transport of the average flow quantities are governed by RANS equations, with the whole range of the scales of turbulence being modeled. Hence, the RANS based modeling approach greatly reduces the required computational effort and resources. They are often used to compute time-dependent flows, whose unsteadiness maybe externally imposed or self-sustained [44].

Reynolds and Favre Averaging

Turbulence can be characterized by fluctuations of all local properties at sufficiently high Reynolds number. Any property f can be split into two parts by Reynolds decomposition

[27]:

$$f = \overline{f} + f' \tag{2.36}$$

where $\overline{f}$ is the mean value, which is a time average over a long period t in the case of steady flow field, while f' is the fluctuation. The mean value is given as:

$$\overline{f} = \frac{1}{t}\int_0^t f(t)'dt' \tag{2.37}$$

The above description is sufficient for constant density flow, for the flows with varying density flows, a mass weighted average method is more widely used:

$$\tilde{f} = \frac{\int_0^t \rho(t')f(t')dt'}{\int_0^t \rho(t')dt'} = \frac{\overline{\rho f}}{\overline{\rho}} \tag{2.38}$$

Thus, any variable could be split into a mean value and a fluctuating value, by the following equation:

$$f = \tilde{f} + f'' \tag{2.39}$$

The RANS equations are obtained by averaging the instantaneous governing equations mentioned earlier through Favre averaging. This approach introduces new stresses, called the Reynolds stresses. This adds a second order tensor of unknowns of which various models can provide different closure levels. RANS is further divided into two broad approaches:

Boussinesq Hypothesis

This method involves using an algebraic equation for the Reynolds stresses which include determining the turbulent viscosity and solving transport equations for determining the turbulent kinetic energy and dissipation. The models include $k - \epsilon$, mixing length and zero

equation models.

Reynolds Stress Model

This approach attempts to solve the transport equations for the Reynolds stresses. Closure for Reynolds stresses require six equations for the six independent Reynolds stresses and another equation for the isotropic turbulence energy dissipation rate. This approach is computationally expensive as it introduces several transport equations for all the Reynolds stresses. More about the turbulence modeling can be found in [44]. The RANS equations are written as:

Continuity

$$\frac{\partial \overline{\rho}}{\partial t} + \frac{\partial (\overline{\rho}\tilde{u}_i)}{\partial x_i} = 0 \tag{2.40}$$

Momentum

$$\frac{\partial \overline{\rho}\tilde{u}_i}{\partial t} + \frac{\partial (\overline{\rho}\tilde{u}_i\tilde{u}_j)}{\partial x_i} = -\frac{\partial \overline{p}}{\partial x_j} + \frac{\partial (\overline{\tau}_{ij} - \overline{\rho}\widetilde{u_i'' u_j''})}{\partial x_i} + \overline{S_{M,i}} \tag{2.41}$$

Energy

$$\frac{\partial \overline{\rho}\tilde{h}_s}{\partial t} + \frac{\partial (\overline{\rho}\tilde{u}_i\tilde{h}_s)}{\partial x_i} = \frac{\partial \overline{p}}{\partial t} - \frac{\partial (\overline{q_i} + \overline{\rho u_i'' h_s''})}{\partial x_i} + \overline{\tau_{ij}\frac{\partial u_i}{\partial x_j}} + \overline{\dot{\omega}}_T + \overline{\dot{Q}} + \overline{S}_H \tag{2.42}$$

Species

$$\frac{\partial \overline{\rho}\tilde{Y}_k}{\partial t} + \frac{\partial (\overline{\rho}\tilde{u}_i\tilde{Y}_k)}{\partial x_i} = -\frac{\partial (\overline{V_{k,i}Y_k} + \overline{\rho}\widetilde{u_i'' Y_k''})}{\partial x_i} + \overline{\dot{\omega}}_k \tag{2.43}$$

where $V_{k,i}$ is the ith component of the diffusion velocity of species k, $\overline{\dot{\omega}}_k$ is the mean reaction rate for species k, $\tilde{h}_s$ is the sensible enthalpy, $\overline{\dot{\omega}}_T$ is the mean heat release rate due to combustion, $\overline{\dot{Q}}$ is the source for heat generation and $\overline{S}_H$ is the source term for the energy equation.

The objective of turbulent modeling is to achieve closures for all unknown terms in a

set of RANS equations. From the above equations, the following terms remain unclosed:

- Reynolds stresses $\overline{\rho}\tilde{u}_i\tilde{u}_j$
- Turbulent fluxes of energy $\overline{\rho u_i'' h_s''}$ and species $\overline{\rho}\widetilde{u_i'' Y_k''}$
- Laminar fluxes of energy $-\overline{\lambda\frac{\partial T}{\partial x_i}}$ species $\overline{V_{k,i}Y_k}$
- Chemical reaction rate $\overline{\dot{\omega}}_k$ and combustion caused heat release $\overline{\dot{\omega}}_T$
- Other source terms $\overline{S}_{M,i}$, $\overline{S}_H$ and $\overline{\dot{Q}}$

Different models are used to identify these unknown terms. The models for Reynolds stresses and chemical reaction rate are called the turbulence model and combustion model respectively. These turbulence models are briefly explained in the following sections. More detailed information about these models can be found in [44].

2.4 Turbulence Modeling

Turbulence models are used to solve for the closure problems, by closing the unknown quantity Reynolds stresses $\overline{\rho}\tilde{u}_i\tilde{u}_j$ in momentum equation. In this section, different turbulent models are briefly introduced. Only the $k-\epsilon$ models have been explained, as the work is based on these models.

Based on the turbulent viscosity hypothesis, the Boussinesq expression, the turbulent Reynolds stresses are generally by analogy with viscous tensor τ_{ij} for Newtonian fluids, given as:

$$\overline{\rho u_i u_j} = \overline{\rho}\tilde{u}_i\tilde{u}_j = -\mu_t\left(\frac{\partial\tilde{u}_i}{\partial x_j} + \frac{\partial\tilde{u}_j}{\partial x_i} - \frac{2}{3}\delta_{ij}\frac{\partial\tilde{u}_i}{\partial x_i}\right) + \frac{2}{3}\overline{\rho}k \tag{2.44}$$

where μ_t is the turbulent dynamic viscosity and is given as:

$$\mu_t = \overline{\rho} C_\mu \frac{k^2}{\epsilon} \tag{2.45}$$

where ϵ is the turbulent energy dissipation rate, C_μ is an empirical constant with a value 0.09 and k is the turbulent kinetic energy, which is given as:

$$k = \frac{1}{2} \sum_{i=1}^{3} \widetilde{u_i'' u_i''} \tag{2.46}$$

2.4.1 Standard k - ϵ Model

Standard k-ϵ model is a two equation closure turbulence model based on kinetic energy and dissipation rate transport equations:

$$\frac{\partial}{\partial t}(\bar{(\rho)}k) + \frac{\partial}{\partial x_j}(\overline{\rho} k \tilde{u}_j) = \frac{\partial}{\partial x_j}\left[(\mu + \frac{\mu_t}{\sigma_k}\frac{\partial k}{\partial x_j})\right] + P_k - \overline{\rho}\epsilon - Y_M \tag{2.47}$$

$$\frac{\partial}{\partial t}(\bar{(\rho)}\epsilon) + \frac{\partial}{\partial x_j}(\overline{\rho} \epsilon \tilde{u}_j) = \frac{\partial}{\partial x_j}\left[(\mu + \frac{\mu_t}{\sigma_\epsilon}\frac{\partial k}{\partial x_j})\right] + C_{\epsilon 1}\frac{\epsilon}{k}P_k - C_{\epsilon 2}\overline{\rho}\frac{\epsilon^2}{k} \tag{2.48}$$

where P_k is the source term in the generation of turbulent kinetic energy due to the mean velocity gradients, calculated by:

$$P_k = \overline{\rho}\widetilde{u_i'' u_i''}\frac{\partial \tilde{u}_i}{\partial x_j} \tag{2.49}$$

Y_M is the contribution of the fluctuating dilatation in compressible turbulence to the overall dissipation rate, which is calculated by:

$$Y_M = 2\rho\epsilon M_t^2 \tag{2.50}$$

where M_t is the turbulent Mach number.

The transport equations have constants $\sigma_k, \sigma_\epsilon, C_{\epsilon 1}, C_{\epsilon 2}$ with the values 1.00, 1.30, 1.44, and 1.92 respectively. $\sigma_k, \sigma_\epsilon$ are the turbulent Prandtl numbers for k and ϵ respectively.

2.4.2 RNG $k-\epsilon$ Model

The RNG $k-\epsilon$ model is similar to the standard $k-\epsilon$ model. But, it has some improvements. This model adds an additional term in its ϵ equation, to increase the accuracy for rapidly strained flows. The transport equations are modified as:

$$\frac{\partial}{\partial t}(\bar{(}\rho)k) + \frac{\partial}{\partial x_i}(\overline{\rho}k\tilde{u}_i) = \frac{\partial}{\partial x_i}\left[(\alpha_k \mu_{eff}\frac{\partial k}{\partial x_i})\right] + P_k - \overline{\rho}\epsilon - Y_M \tag{2.51}$$

$$\frac{\partial}{\partial t}(\bar{(}\rho)\epsilon) + \frac{\partial}{\partial x_j}(\overline{\rho}\epsilon\tilde{u}_j) = \frac{\partial}{\partial x_j}\left[(\alpha_\epsilon \mu_{eff}\frac{\partial k}{\partial x_j})\right] + C_{\epsilon 1}\frac{\epsilon}{k}P_k - C_{\epsilon 2}\overline{\rho}\frac{\epsilon^2}{k} - R_\epsilon \tag{2.52}$$

where α_k and α_ϵ are the inverse effective Prandtl numbers, the values of model constants, $C_{\epsilon 1}, C_{\epsilon 2}$ are changed to 1.42 and 1.68 respectively.

The additional term, which made the difference, R_ϵ is computed from the following equation:

$$R_\epsilon = \frac{C_\mu \rho \eta^3(1-\eta/\eta_0)}{1+\beta\eta^3}\frac{\epsilon^2}{k} \tag{2.53}$$

where $\eta = \sqrt{S_{ij}S_{ij}}k/\epsilon, \eta_0 = 4.38, \beta = 0.012$.

2.5 Realizable $k-\epsilon$ Model

Standard k-ϵ model performs well for boundary layer problems. But, when there is any flow separation, vortex breakdown, swirling or any recirculation, it does not provide with

superior results. These flow phenomena are over predicted at times by the standard k-ϵ. To improve this drawback, Shih et. al[45] came up with Realizable k-ϵ model. It's performance is superior to the standard k-ϵ especially when the flow has spreading jets, recirculation, massive flow separation and boundary layers under the influence of strong adverse pressure gradients. It captures the mean flow of very complex geometries with a greater accuracy. It exhibits superior performance for the flows with low to moderate swirl better than any other RANS turbulence models. This model differs from the standard model in two ways [44] :

- Realizable k-ϵ model has an alternative formulation for the turbulent viscosity
- Dissipation rate, ϵ has a modified transport equation which is derived from an equation for the transport of mean-square vorticity fluctuation

The transport equation of the turbulent kinetic energy and the modified transport equation for the eddy dissipation are:

$$\frac{\partial}{\partial t}(\overline{\rho}k) + \frac{\partial}{\partial x_j}(\overline{\rho}k\tilde{u}_j) = \frac{\partial}{\partial x_j}\left[(\mu + \frac{\mu_t}{\sigma_k}\frac{\partial k}{\partial x_j})\right] + P_k - \overline{\rho}\epsilon - Y_M \tag{2.54}$$

$$\frac{\partial}{\partial t}(\overline{\rho}\epsilon) + \frac{\partial}{\partial x_i}(\overline{\rho}\epsilon\tilde{u}_i) = \frac{\partial}{\partial x_i}\left[(\mu + \frac{\mu_t}{\sigma_\epsilon}\frac{\partial \epsilon}{\partial x_i})\right] + \overline{\rho}C_1 S_\epsilon - \overline{\rho}C_2\frac{\epsilon^2}{k + \sqrt{\nu\epsilon}} \tag{2.55}$$

where $C_1 = max[0.43, \frac{\eta}{\eta+5}]$, $\eta = S\frac{k}{\epsilon}$ *and* $S = \sqrt{2S_{ij}S_{ij}}$. Y_M is the fluctuating dilatation in compressible turbulence to the dissipation rate. C_2 is the constant in the equation and has the value, 1.9. σ_k and σ_ϵ, with the the values 1 and 1.2, are the turbulent Prandtl numbers for k and ϵ respectively. S_ϵ is the source term defined by the user.

From the two equations, k and ϵ, the k-equation for all the k-ϵ models, standard, RNG and realizable, is same, except for the constants. The eddy viscosity like the other k-ϵ is

computed from the equation:

$$\mu_t = \rho C_\mu \frac{k^2}{\epsilon} \tag{2.56}$$

C_μ, which is a constant in the standard and RNG k-ϵ, in the above equation is not constant in the realizable model. This is the major variation from the other two models. It is a function of mean strain and rotation rates, the angular velocity of the system rotation, and the turbulence fields. It is computed from

$$C_\mu = \frac{1}{A_0 + A_s \frac{kU^*}{\epsilon}} \tag{2.57}$$

where

$$U^* = \sqrt{S_{ij} S ij + \widetilde{\Omega_{ij}} \widetilde{\Omega_{ij}}} \tag{2.58}$$

and

$$\widetilde{\Omega_{ij}} = \Omega_{ij} - 2\epsilon_{ijk}\omega_k$$

$$\Omega_{ij} = \overline{\Omega_{ij}} - \epsilon_{ijk}\omega_k$$

$\overline{\Omega_{ij}}$ is the mean rate of rotation tensor in a rotating frame of reference, which is rotating at an angular velocity ω_k. A_0 and A_s are the default model constants with the values 4.04 and $\sqrt{6}\cos\phi$ respectively, where

$$\phi = \frac{1}{3}\cos^{-1}(\sqrt{6}W), \quad W = \frac{S_{ij}S_{jk}S_{kl}}{\tilde{S}^3}, \quad \tilde{S} = \sqrt{S_{ij}S_{ij}}, \quad S_{ij} = \frac{1}{2}(\frac{\partial u_j}{\partial x_i} + \frac{\partial u_i}{\partial x_j})$$

2.6 Premixed Combustion Modeling in Fluent

In premixed combustion, the fuel and the oxidizer are mixed before the combustion chamber. This premixing results in a homogeneous mixture of the fuel and the air. Fluent has more flexibility when modeling premixed combustion, as it has multiple models to simulate the combustion. This section explains briefly about the available models and more about the model that is adapted for the current study.

2.6.1 Premixed Combustion Model

Premixed turbulent combustion model is an easy and a straight forward approach for modeling premixed combustion. This model is based on a reaction-progress variable, c, approach. There are two sub-models in this premixed combustion model: Zimont model and extended coherent flamelet model (ECFM). Both the models have their own advantages.

Zimont model

In Zimont's model [44], the propagation of flame front is modeled by solving a transport equation for the mean progress variable ,c. The transport equation is given as:

$$\frac{\partial}{\partial t}(\rho c) + \nabla \cdot (\rho \tilde{v} c) = \nabla \cdot (\frac{\mu_t}{S c_t} \nabla c) + \rho S_c \tag{2.59}$$

where c is the mean reaction variable, $S c_t$ is the turbulent Schimdt number and S_c is the reaction progress source term. The reaction progress variable is defined as the normalized

sum of the product species and is given as:

$$c = \frac{\sum_{i=i}^{n} Y_i}{\sum_{i=1}^{n} Y_{i,eq}} \tag{2.60}$$

where n is the number of products, Y_i is the mass fraction of the i^{th} product species i and $Y_{i,eq}$ is the equilibrium mass fraction of the i^{th} product species. Since, c is defined as a fraction, it ranges between 0 and 1. If $c = 0$, then the mixture is defined as the unburnt mixture and if $c = 1$, then the mixture is assumed to be a burnt mixture. Usually, c is defined at the boundaries. The mean reaction rate in Zimont's model is computed from:

$$\rho S_c = \rho_u U_t |\nabla c| \tag{2.61}$$

where ρ_u is the density of the unburnt mixture and U_t is the turbulent flame speed. The turbulent flame speed, U_t is one of the important factors in modeling the premixed turbulent combustion. More about Zimont model can be found in the references [44] [46] [47] .

Enhanced Coherent Flamelet Model

The Enhanced coherent flamelet model (ECFM) [44] is more refined pre-mixed combustion model than the Zimont model, and theoretically, it has a greater accuracy. But, computationally it is very expensive and less robust. The ECFM model solves an additional equation for flame area density, Σ, which later is used to calculate the mean reaction rate as mentioned in Zimont's transport equation.Transport of the net flame per unit volume, or the flame area

density, Σ is given as:

$$\frac{\partial \Sigma}{\partial t} + \nabla \cdot (\tilde{v}\Sigma) = \nabla \cdot (\frac{\mu_t}{S\, c_t} \nabla(\frac{\Sigma}{\rho})) + (P_1 + P_1 + P_3)\Sigma - D \tag{2.62}$$

where P_1 is the source due to turbulence interaction, P_2 is the source due to dilatation in the flame, P_3 is the source due to expansion of burnt gas and D is the dissipation of flame area. The mean reaction rate can be calculated from:

$$\rho S_c = \rho_u U_l \Sigma \tag{2.63}$$

where U_l is the laminar flame speed. More information about the sources and the flame are dissipation can be found in [48] [44].

Even though premixed combustion model is a straight forward advantageous model, it has some limitations which refrains the usage of this model more frequently. These limitations include [44]:

- The premixed combustion model cannot be used with the density based solver. Hence, it can be only used with the pressure based solver.
- It is valid only for turbulent and subsonic flows.
- It fails to calculate the species mass fractions and cannot be used along with the pollutant models.
- It cannot be used to simulate the reacting discrete-phase particles, as this results in a partially premixed system.

However, it can efficiently predict the flame front propagation. This model can be used if the

main focus is on the flame front propagation not on the species mass fractions.

2.6.2 Species Transport for Premixed Combustion

Proper modeling of species transport is required to model mixing or reaction. Fluent can model the mixing and transport of species by solving the conservation equations describing diffusion, convection and sources of reaction for each individual species. Multiple simultaneous reactions can be modeled, with these reactions occurring in bulk/volumetric or wall or surface of the particles. Species transport model can be used to simulate both reacting and non-reacting flows based on the given inputs [44]. Fluent solves a convection-diffusion equation to predict the local mass fractions of individual chemical species. The equation is given as:

$$\frac{\partial}{\partial t}(\rho Y_i) + \nabla \cdot (\rho \tilde{v} Y_i) = -\nabla \cdot \vec{J}_i + R_i + S_i \tag{2.64}$$

where R_i is the net rate of production of species i, S_i is the rate of creation by addition from the dispersed phase including any other sources, and $\vec{J}_i$ is the diffusion flux of species i, arises due to the presence of concentration gradients. For laminar flows,the mass diffusion or the diffusion flux is given as:

$$\vec{J}_i = -\rho D_{i,m} \nabla Y_i \tag{2.65}$$

$D_{i,m}$ is the diffusion coefficient for species i in the mixture.

Mass diffusion in the turbulent flows can be calculated using:

$$\vec{J}_i = -(\rho D_{i,m} + \frac{\mu_t}{S c_t}) \nabla Y_i \tag{2.66}$$

Here in the equation, $S c_t$, is the Schimdt number, which is a ratio of turbulent viscosity, μ_t and

turbulent diffusivity, D_t.

The main focus will be on the bulk phase or the volumetric reactions.There are four sub-models under volumetric reactions in species transport, among them, one is a hybrid model.

Laminar Finite Rate Model

The laminar finite-rate model calculates the reaction rates and chemical source terms using Arrhenius relations. This model doesn't consider the effect of the turbulent fluctuations. The model is apt for the laminar flames and can be less accurate for turbulent flames as the Arrhenius chemical kinetics is highly non-linear. However, it can be used to model small turbulence chemistry interactions.

The net source of chemical species i due to reaction is computed as the sum of the Arrhenius reaction sources:

$$R_i = M_{w,i} \sum_{r=1}^{N_R} \hat{R}_{i,r} \tag{2.67}$$

where $M_{w,i}$ is the molecular weight of ith species, $\hat{R_i}$, r is the Arrhenius molar production/dissipation rate of ith species in reaction r and N_R is the number of reactions. The rth reaction can be written as:

$$\sum_{i=1}^{N} \nu'_{i,r} M_i \underset{k_{b,r}}{\overset{k_{f,r}}{\rightleftharpoons}} \sum_{i=1}^{N} \nu''_{i,r} M_i \tag{2.68}$$

where N is the number of chemical species, $\nu'_{i,r}$ and $\nu''_{i,r}$ are the stoichiometric coefficients for reactant and product i in reaction r respectively, M_i is the individual species i, $k_{f,r}$ and $k_{b,r}$ are the forward and backward rate constants for the reaction r respectively.

The above equation is valid for both reversible and irreversible reactions. For an irreversible reaction, the backward rate constant, $k_{b,r}$, is omitted. The molar rate of produc-

tion/dissipation of species i in reaction r is given as:

$$\hat{R}_{i,r} = \Gamma(\nu''_{i,r} - \nu'_{i,r})\left(k_{f,r}\prod_{j=1}^{N}[C_{j,r}]^{(\eta'_{j,r}+\eta''_{j,r})}\right) \tag{2.69}$$

where $C_{j,r}$ is the molar concentration of species j in reaction r with units $kgmol/m^3$, $\eta'_{j,r}$ and $\eta''_{j,r}$ are the rate exponents for jth reactant and product species in reaction r, and Γ is the net effect of third bodies on the reaction rate. This term is same for both reversible and irreversible reactions. It is given as:

$$\Gamma = \sum_{j}^{N}\gamma_{j,r}C_j \tag{2.70}$$

where $\gamma_{j,r}$ is the third body efficiency of species j in reaction r.

The molar rate of production/dissipation of species j in reaction r for a reversible reaction is given as:

$$\hat{R}_{i,r} = \Gamma(\nu''_{i,r} - \nu'_{i,r})\left(k_{f,r}\prod_{j=1}^{N}[C_{j,r}]^{\eta'_{j,r}} - k_{b,r}\prod_{j=1}^{N}[C_{j,r}]^{\nu''_{j,r}}\right) \tag{2.71}$$

The rate exponent of the reverse reaction is always the stoichiometric coefficient of the product species.

The forward rate constant for the reaction r, $k_{f,r}$ is computed from the following Arrhenius expression:

$$k_{f,r} = A_r T^{\beta_r} e^{\frac{-E_r}{RT}} \tag{2.72}$$

where A_r is the pre-exponential factor, β_r is the temperature exponent, E_r is the activation energy for the reaction and R is the universal gas constant.

Similarly, for a reversible reaction, the backward rate constant is given as:

$$k_{b,r} = \frac{k_{f,r}}{K_r} \tag{2.73}$$

where K_r is the equilibrium constant for the rth reaction, computed using the following equation:

$$K_r = \exp\left(\frac{\Delta S_r^0}{R} - \frac{\Delta H_r^0}{RT}\right)\left(\frac{p_{atm}}{RT}\right)^{\sum_{i=1}^{N}(\nu''_{i,r}-\nu'_{i,r})} \tag{2.74}$$

where S_r^0 and H_r^0 are the standard-state entropy and standard-state enthalpy of the reaction r respectively p_{atm} is the atmospheric pressure. The term in the exponential function is the change in Gibbs free energy and the components are computed as follows:

$$\frac{\Delta S_r^0}{R} = \sum_{i=1}^{N}(\nu''_{i,r} - \nu'_{i,r})\frac{S_i^0}{R} \tag{2.75}$$

$$\frac{\Delta H_r^0}{R} = \sum_{i=1}^{N}(\nu''_{i,r} - \nu'_{i,r})\frac{h_i^0}{RT} \tag{2.76}$$

where S_i^0 and h_i^0 are the standard-state entropy and standard-state enthalpy or the heat of formation respectively.

Eddy-Dissipation Model

The Eddy-Dissipation model, which focuses on the turbulent-chemistry interaction, is based on the work of Magnussen and Hjertager [49]. Since, most of the fuels burn very quickly, the reaction rate is controlled by turbulent mixing.

The net rate of production of species i of reaction r is given by the smaller of the two

following expressions:

$$R_{i,r} = \nu'_{i,r} M_{w,i} A \rho \frac{\epsilon}{k} \min_{R} \left(\frac{Y_R}{\nu'_{R,r} M_{w,R}} \right) \tag{2.77}$$

$$R_{i,r} = \nu'_{i,r} M_{w,i} A B \rho \frac{\epsilon}{k} \frac{\sum_P Y_P}{\sum_j^N \nu''_{j,r} M_{w,j}} \tag{2.78}$$

where Y_P is the mass fraction of product species, P, Y_R is the mass fraction of reactant species, R, A and B are empirical constants with the values 4.0 and 0.5 respectively.

From the above two equations, it is evident that the chemical reaction rate is governed by the large-eddy mixing time scale, k/ϵ. Combustion starts whenever the turbulence is present ($i.e., k/\epsilon > 0$) and an ignition source is not required to initiate the combustion.

Finite-Rate/Eddy-Dissipation Model

In premixed combustion, the reactant mixture can ignite even before the flame stabilizer. To counteract this issue, a new model has been made available in ANSYS Fluent, i.e.,finite-rate/eddy-dissipation model. The finite-rate/eddy-dissipation model is a hybrid of finite-rate model and the eddy-dissipation model. In this model reaction rates from both the models are calculated and the net reaction rate is taken as the minimum of these two rates. The Arrhenius rate acts as a kinetic switch, preventing the reaction happening before the flame stabilizer. Once the combustion gets started, the eddy-dissipation rate is smaller than the Arrhenius rate, and the reactions are mixing limited.

Eddy-Dissipation Concept Model

The eddy-dissipation concept model (EDC) is an extension of the eddy-dissipation model, which considers detailed chemical mechanisms in turbulent flows. It assumes that reaction occurs in small turbulent scales, the fine scales. The length fraction of the fine scales is

given as:

$$\xi^* = C_\xi \left(\frac{\nu\epsilon}{k^2}\right)^{1/4} \tag{2.79}$$

where C_ξ is the volume fraction, which is a constant with a value of 2.1377 and $/nu$ is the kinematic viscosity.The volume fraction of the fine scales is calculated as ξ^{*^3}. Species are assumed to react in the fine structures over a time scale:

$$\tau^* = C_\tau \left(\frac{\nu}{\epsilon}\right)^{1/2} \tag{2.80}$$

C_τ is a time scale constant which is equal to 0.4082.

The source term in the conservation equation for the mean species i, equation is modeled as:

$$R_i = \frac{\rho(\xi^*)^2}{\tau^*[1-(\xi^*)^3]}(Y_i^* - Y_i) \tag{2.81}$$

where Y_i^* is the fine scale species mass fraction after reacting over the time τ^*.

Even though, the EDC model is used for detailed chemical mechanisms in turbulent reacting flows, the mechanisms are invariably stiff and their numerical integration is computationally expensive. So, the model should be used only when the assumption of fast chemistry is invalid.

2.6.3 Flamelet Generated Manifold

Flamelet generated manifold (FGM) is used as reduction technique for modeling combustion. FGM assumes that the local flame structures in a 3-dimensional turbulent flame look like the flamelets. So, the FGM is a mix of flamelet - manifold methods. FGM parameterizes all the thermo-chemical variable by a few control variables like reaction progress - c,

mixture fraction - f, and scalar dissipation - χ. FGM database has a lot of flamelets and these flamelets have their own boundary conditions. Fluent generates the 1-dimensional premixed flamelets and solves them in reaction progress space. Flamelet equations are given as,

$$\rho\frac{\partial Y_k}{\partial t} + \frac{\partial Y_k}{\partial c}\dot{\omega}_c = \rho\chi_c\frac{\partial^2 Y_k}{\partial c^2} + \dot{\omega}_k \tag{2.82}$$

$$\rho\frac{\partial T}{\partial t} + \frac{\partial T}{\partial c}\dot{\omega}_c = \rho\chi_c\frac{\partial^2 T}{\partial c^2} - \frac{1}{c_p}\sum_k h_k\dot{\omega}_k + \frac{\rho\chi_c}{c_p}\left(\frac{\partial c_p}{\partial c} + \sum_k c_{p,k}\frac{\partial Y_k}{\partial c}\right)\frac{\partial T}{\partial c} \tag{2.83}$$

$$\chi_c = \frac{\lambda}{\rho c_p}|\nabla c|^2 \tag{2.84}$$

where ρ is the density of the fluid, t is the time, Y_k is the mass fraction of the k^{th} species, T is the temperature, $\dot{\omega}_k$ is the mass reaction rate of the species, h_k is the total enthalpy, $c_{p,k}$ is the specific heat of the k^{th} species at constant pressure and λ is the thermal conductivity.

χ_c is a function of c, and is given as,

$$\chi_c(c) = \chi_{max}exp(-2(erfc^{-1}(2c))^2) \tag{2.85}$$

where χ_{max} is maximum scalar dissipation specified by the user and $erfc^{-1}$ is the inverse complimentary inverse function.

In general, if a 1-dimensional flamelet is calculated at an equivalence ratio, then it will also correspond to the mixture fraction, f. At any mixture fraction, f, the scalar dissipation, is modeled as,

$$\chi_c(f,c) = \chi_{max}^{sto}exp(-2(erfc^{-1}(\frac{f}{f_{sto}}))^2)exp(-2(erfc^{-1}(2c))^2) \tag{2.86}$$

where χ_{max}^{sto} is the scalar dissipation at stoichiometric mixture fraction. It has a default value of

1000 1/s, which gives a reasonable solution at all equivalence ratios at normal temperature and pressure.

Chapter 3

Numerical Methodology

This chapter discusses the actual experimental setup that is used to model a numerical setup, problem statement and the numerical methodologies used for the validation study. The computations are based on the behavior of the flow in the cylindrical chamber with a swirler, followed by a sudden expansion. The study uses Reynolds Averaged Navier-Stokes (RANS) equations for modeling the reacting and non-reacting flow in steady conditions.

3.1 Experimental Setup

The numerical study is carried out on an experimental setup shown in figure 3.1. This is adapted from King Abdulla University of Science and Technology (KAUST, Saudi Arabia) It has a burner which generates swirl stabilized flame with the help of a radial swirler. At an equivalence ratio of 0.67, a mixture of methane and air is fed to to the burner by a mixing chamber, which the mixture is mixed thoroughly. The mixture is fed into a 120 mm long plenum with the help of two tubes and it goes through a 20 mm long honeycomb to breakdown the large turbulent structures in the flow. There is a radial swirler just before the

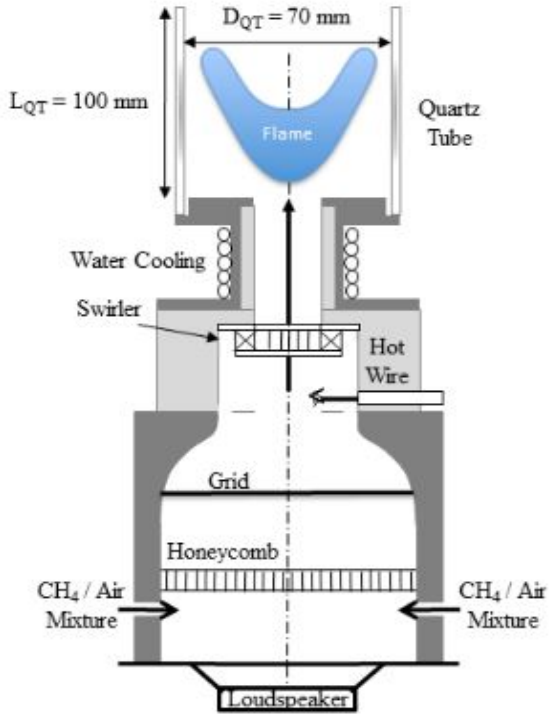

Figure 3.1: Experimental setup equipped with a swirler [14]

burner. There are twelve identical swirler blades that are angled at 30^0 with respect to the central axis . This radial swirler provides the much needed swirl with a swirl number 0.38, and this swirl is considered to be a moderate swirl. The axial velocity at the exit of the injection tube is approximately, 7 m/s. The flame with a thermal power of 4 kW, is enclosed by a quartz tube, which is 70 mm in diameter. A detailed description of the burner can be found in [50]

Problem Statement:

The current work focuses on the study of flow behavior in non-reacting and reacting flows in a lean premixed combustor and validate the numerical results with the experimental results obtained from the works of Sabatino et al [14], and LES results by Maestro et al [3]. Analyses are conducted to study the effect of swirl number and a cylindrical central rod in premixed swirl stabilized combustion. All the computations are performed using Reynolds Averaged Navier-Stokes equations (RANS) in ANSYS Fluent with the help of Ohio Supercomputer Center's resources [51].

3.2 Numerical Setup

A numerical study is carried out on the lean premixed swirl stabilized combustion, based on the geometry from the experimental setup. The 3-D geometry for the numerical study is shown in 3.1. The flow domain can be split into four sections, plenum, swirler, injection tube, and quartz tube or the combustion chamber sections, in the direction of the flow respectively. The swirler is a radial swirler, where the flow enters in radial direction. It has 12 identical blades with an edge angle of 30^0. The geometry was modeled in Solidworks and it was exported to ANSYS Workbench. Meshing for this geometry was done using ANSYS Mesh. The origin for the geometry is at the center of the inlet, with 'y' being the axial or flow direction, 'x' being the radial direction and 'z' being the tangential direction. All the dimensions were normalized by the swirler's exit diameter, which is d = 18mm. Figure 3.2 shows the Solidworks model of the fluid domain and Figure 3.3 shows the dimensions of the fluid domain in front and isometric views. All the dimensions mentioned in the figure are in millimeters.

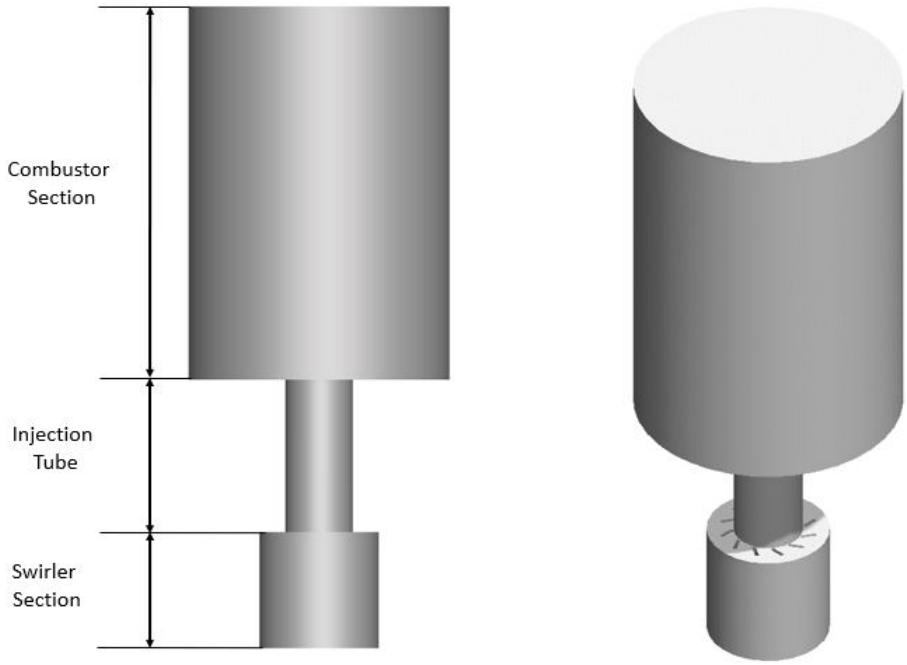

Figure 3.2: Solidworks models of the fluid domain in front view and isometric view

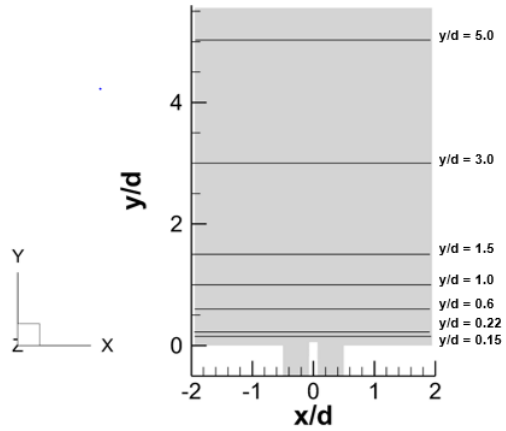

Figure 3.4: Different axial locations in the combustion chamber

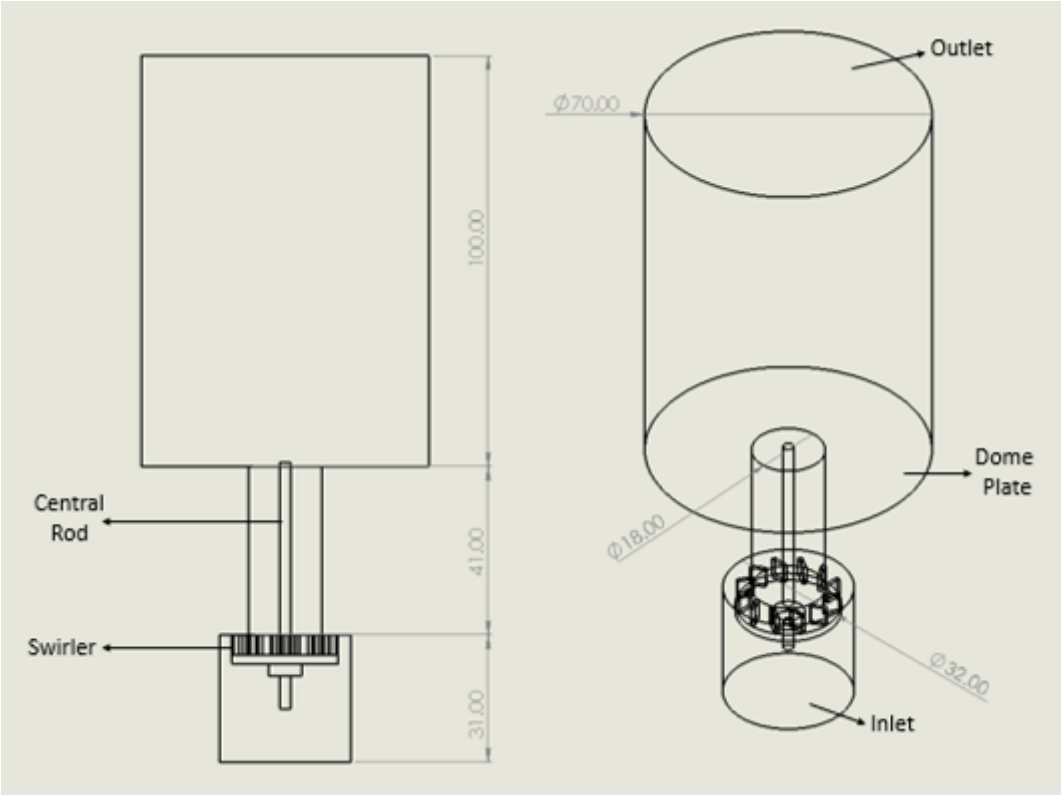

Figure 3.3: Dimensions of the fluid domain in front view and isometric view

Figure 3.4 shows the various axial locations where the results are analyzed. In this study, 'x' represents the radial direction, 'y' corresponds to the axial or flow direction and 'z' is the tangential direction.

3.3 Solver Setup

The Reynolds Averaged Navier-Stokes equations (RANS) are solved using the commercial code Fluent, with versions 18.1 and 18.2. This code solves the continuity, momentum, energy, species and turbulence equations altogether for the Navier-Stokes equations. The mass flow rate at the inlet is approximately $2g/s$, temperature and pressure are 300 K and 1 atm respectively. The Reynolds number was calculated based on the inlet diameter and the value is 4800.

In Fluent, there are two types of solvers, pressure-based and density-based solvers. The density-based solver is used for the flows that are supersonic. Pressure-based solver is used for subsonic flows. For the current study, a pressure based solver is used for the computations, as the flow is subsonic. Based on the time dependence, the flow is chosen as either steady or transient.

3.3.1 Models

Viscous Model

There are various types of viscous models that are available in Fluent. These models include, inviscid, laminar, Spalart-Allmaras, k-ϵ, k-ω, shear stress model (SST), Reynolds stress model (RSM), scale adaptive simulation (SAS), detached eddy simulation (DES), large eddy simulation (LES). Among these models, the k-ϵ models are explained in the previous chapter. For the current study, realizable k-ϵ model with standard wall functions has been chosen. As the model is computationally inexpensive and provides the results with better accuracy for the low swirl flows, than any other RANS models that are available. All the constant values

associated with the model are chosen as default values.

Species Model Chemistry

A partially premixed combustion model is considered modeling non-reacting flow with the actual species, and the premixed combustion by neglecting the diffusion. In the partially premixed combustion, FGM model is used for modeling chemistry. ANSYS Fluent, provides multiple options to calculate the flamelets and the PDF table, turbulence-chemistry interactions. Flamelets can be calculated either by a premixed or a diffusion approach. Since the study is focused on premixed combustion, the premixed approach is chosen and the flamelets are calculated non-adiabatically. This non-adiabatic approach considers the fluid's enthalpy for generating the PDF look-up table and calculating the flame temperature. The size of the table ($f \times c$) is considered as 32×32, which is based on the number of grid points in the mixture fraction space and the reaction progress space. The grid points in mixture fraction space specifies the number of mixture fraction grid points distributed between the oxidizer ($f = 0$) and the fuel ($f = 1$). Similarly, the grid points in the reaction progress space specifies the number of reaction progress grid points distributed between unburnt ($c = 0$) and the burnt ($c = 1$) states. Increasing the resolution of the table provides greater accuracy. But, the solution time and the memory requirements also increase with these grid points.

The scalar dissipation at stoichiometric mixture fraction, which specifies the premixed flamelet strain rate, was set to a default value of $1000Hz$. This value provides good results for most of the premixed flames. The turbulence-chemistry interaction can be calculated by finite-rate model or turbulence flame speed model or a combination of both. For the current study, the combination of the finite-rate model and turbulent flame speed model (Zimont/Peters) was considered and the model uses the minimum of the two reaction rates. Also,

the finite rate model acts as a kinetic switch and prevents the combustion to occur before the flame stabilizer. The source term variance was calculated using the transport equation, which gave more realistic results. For modeling chemistry, the Gas Research Institute mechanism 3.0, GRI-Mech 3.0 [52], with 325 elementary reactions between 53 species with hydrocarbons up to propane, was used. The presence of higher hydrocarbons helps to describe the hydrocarbon recombination in fuel rich regions. A summary of the FGM parameters, that are used for the current study, are tabulated in the Table 3.1.

Parameter	Approach/Value
Flamelet	Premixed
Flame Temperature Calculation	Non-adiabatic
Table Grid Size	32×32
Scalar Dissipation [Hz]	1000
Mean Source Term	Finite-Rate and Turbulent Flame Speed
Variance	Transport Equation

Table 3.1: Summary of the FGM parameters

Initial and Boundary Conditions

The operating conditions that are used for the initialization of numerical solution, are tabulated in the Table 3.2. Velocity at the inlet and pressure boundary at the outlet are considered for simulation, and flow is assumed as normal to the boundary. The inlet and the outlet pressure are considered to be 1 atm. For the turbulence specification, a turbulent intensity of 5% and a turbulent viscosity ratio of 10 are used at both inlet and outlet. Temperatures at these boundaries are at 300 K. When modeling the reacting flow with an equivalence ratio of 0.67, the mass/mole fractions of the species are specified based on the methane-air global

reaction, which is given as:

$$CH_4 + 2.985(O_2 + 3.76N_2) => CO_2 + 2H_2O + 0.985O_2 + 11.2236N_2 \quad (3.1)$$

The respective mole fractions of the species: On the reactants side $CH_4 = 0.0657, O_2 = 0.196, N_2 = 0.7383$, on the products side, $CO_2 = 0.0657, H_2O = 0.1313, O_2 = 0.0647, N_2 = 0.7383$

Condition	Mass flow rate	Temperature	Pressure	Turbulent intensity	Turbulent Viscosity ratio
Value	2.0579 g/s	300 K	1 atm	5%	10

Table 3.2: Operating conditions

Solution/Discretization Methods

The pressure-based solver allows the user to solve the flow problem either in a coupled or segregated manner. The pressure-velocity coupling is a numerical algorithm which uses continuity and momentum equations to derive an equation for pressure. The pressure-velocity coupling can be done by Semi-Implicit Method for Pressure-Linked Equations (SIMPLE), Simple-Consistent (SIMPLEC), Pressure-Implicit with Splitting of Operators (PISO), Coupled and Fractional Step Method (FSM) algorithms. Among these five algorithms, SIMPLE is chosen for pressure-velocity coupling, along with a least squares cell based gradient method and standard pressure. This algorithm uses a relationship between velocity and pressure corrections to calculate the pressure field. Discretization is the process of solving algebraic equations, instead of differential equations, at discrete points. Accuracy of a solution depends on the order of the discretization. It increases with the increase in the order. For a better convergence of the solution, momentum, turbulent kinetic energy and turbulent dissipation rate equations are solved with first order upwind scheme. After few iterations, the discretization

methods are changed to second order. This way, the solution converges efficiently with better accuracy. For the current study, both spatial discretization and temporal discretization are solved using the second order upwind scheme.

Residuals and Convergence Criterion

Convergence of a solution is obtained, if all the conservation equations obeyed at all the elements to a specified tolerance, residual, or if the solution does not change with the subsequent equations. A decrease in the residuals at least by three orders of magnitude indicates an acceptable convergence. For a transient case, the residuals should decrease at least by three orders of magnitude in each iteration. For a pressure-based solver, the energy residual has to reduce to an order of 10^{-6} and the species residual should decrease to 10^{-5} to achieve the species balance.In the current study, all the residuals, continuity, momentum, turbulence, and species are employed with a convergence criteria in the order of 10^{-5}. For energy, the convergence is achieved if the residual reaches 10^{-6} or less than that.

Initialization

Procedures with a lot of iterations require all the solution variables to be initialized before calculating a solution. A better and realistic initial values improves the solution's stability and convergence. For the current study, the flow problem is initialized from the inlet. For certain variables, specific values can be patched as an initial guess using cell registers by marking the cells. Especially, when modeling combustion, the reacting zone is patched with very high temperature, equal to the adiabatic flame temperature of the fuel, and reactant and product species, to initiate the combustion or with the reaction progress variable, c. In this work, for methane-air combustion, the reaction zone is patched with the reaction progress variable with

'1'. This patch acts a ignition spark to initiate the chemical reaction.

3.3.2 Error Methodology

Error in the true value and the measured value is estimated using L2 or Euclidean norm. L2 norm is calculated by the following expression[53],

$$||l||_2 = \sqrt{\sum_{i=1}^{n} l_i^2} \tag{3.2}$$

where l_i is the i^{th} data point of the parameter l, n is the total number of data points. Using this L2 norm, error can be discretized as absolute and relative. They are given as,

$$\text{Absolute error} = ||l_{approx} - l_{true}|| \tag{3.3}$$

$$\text{Relative error} = \frac{||l_{approx} - l_{true}||}{||l_{true}||} \tag{3.4}$$

where l_{approx} and l_{true} are the approximate and true values of the parameter l respectively. Assuming $||l_{true}||$ is not equal to zero.

3.3.3 Mesh Generation and Refinement Study

The meshing is done using ANSYS Mesh. The flow domain is partitioned into a large number of finite smaller elements. All the flow properties like the velocity, pressure, temperature etc., are calculated at these smaller elements. So, if the mesh is finer, the number elements will be increased. This gives scope to obtain a solution with greater accuracy. But, a very fine mesh is computationally expensive and requires a lot of time to get the convergence.

An unstructured mesh, with tetrahedral elements, is employed for the current study. Body sizing tool is used to generate mesh to the entire geometry. The areas where the recirculation zone is observed, have a fine mesh.

Achieving a good solution depends on the type of mesh used in a simulation. Mesh refinement study has to be conducted while simulating a problem to check if the solution is dependent on the fineness of the mesh. For the current study, from the exit of the burner till $2d$ downstream of the combustion chamber is considered for the refinement. The smallest cell size in the mesh is $1X10^{-4}$. This is based on the Taylor microscale which is $9.5X10^{-4}$ L2 norm of the normalized axial and tangential velocities, obtained from the velocity profiles at $y/d = 0.2\overline{2}$, are the considered parameters for calculating the relative error between the meshes. Based on the grid refinement ratio, r, of 1.5, 3 meshes are considered for the study - 4.29, 6.44 and 9.66 million tetrahedral unstructured meshes. Figure 3.5 shows the normalized axial and tangential velocity profiles at $y/d = 0.2\overline{2}$ for 3 meshes. Relative errors between the three meshes are tabulated in table 3.3. The change from coarse mesh to medium is noticeable. But, when the mesh is refined further from medium to fine, the change is very minute. Based on this mesh refinement study, 6.44M (medium) unstructured tetrahedral mesh is considered. Figure 3.6 shows the mid-plane section of the mesh, that is used for the current study.

		Relative Error in V_y/V_{in}	Relative Error in V_z/V_{in}
Mesh Refinement	Coarse (4.29M) to Medium (6.44M)	0.0602	0.0681
	Medium (6.44M) to Fine (9.66M)	0.0093	0.0084

Table 3.3: Relative errors in V_y/V_{in} and V_z/V_{in} between 3 meshes - 4.29M, 6.44M, 9.66M

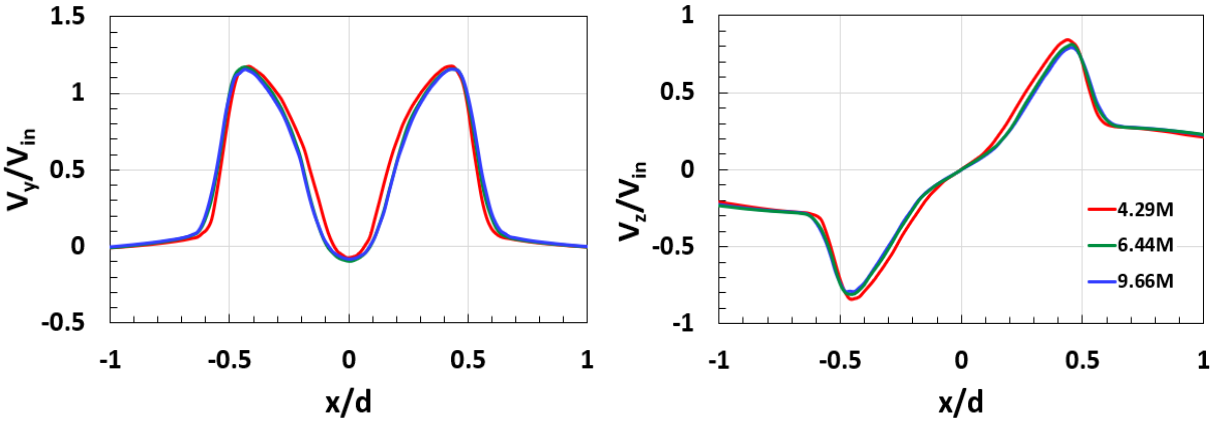

(a) Axial velocity **(b)** Tangential velocity

Figure 3.5: Comparison of velocity profiles, at $y/d = 0.2\overline{2}$, between 3 meshes - 4.29M, 6.44M, 9.66M

Figure 3.6: 6.44M unstructured tetrahedral mesh in xy-plane used for non-reacting and reacting flows

3.4 Combustion Regime

Table 3.4 shows the parameters that are used to define the regime in premixed combustion. In this study, Damkhler number, Da, is greater than 1, which implies a faster chemistry. Here, Karlovitz number, Ka, is less than 1, and this indicates that the flame is less thicker than the Kolmogorov length scale. On the combustion diagram, the regime falls under wrinkled and corrugated flames. If the flame is in less turbulence, then it will be wrinkled. The corrugated flame regime represents a flame in high turbulence with a higher turbulent velocity than the flame speed. In the current study, the turbulent velocity is greater than the laminar flame speed.

So, the flame is a corrugated flame. Figure 3.7 shows the location of the combustion regime in modified Borghi - Peters combustion diagram [5], for the current study. The red colored patch is the location of the combustion regime. In both the flame regimes, wrinkled and corrugated, the flame front is considered as ensemble of flamelets.

	Parameter	Value
	Laminar flame speed (m/s)	0.153
	Laminar flame thickness (m)	9.51×10^{-5}
Integral turbulent scales	Length (m)	2.24×10^{-3}
	Time (s)	6.27×10^{-3}
	Velocity (m/s)	0.357
Small turbulent scales (Kolmogorov)	Length (m)	1.0×10^{-4}
	Time (s)	6.91×10^{-4}
	Velocity (m/s)	0.145
Dimensionless numbers	Turbulent Reynolds number	55
	Damköhler number	7
	Karlovitz number	0.9

Table 3.4: Turbulent premixed combustion regime parameters

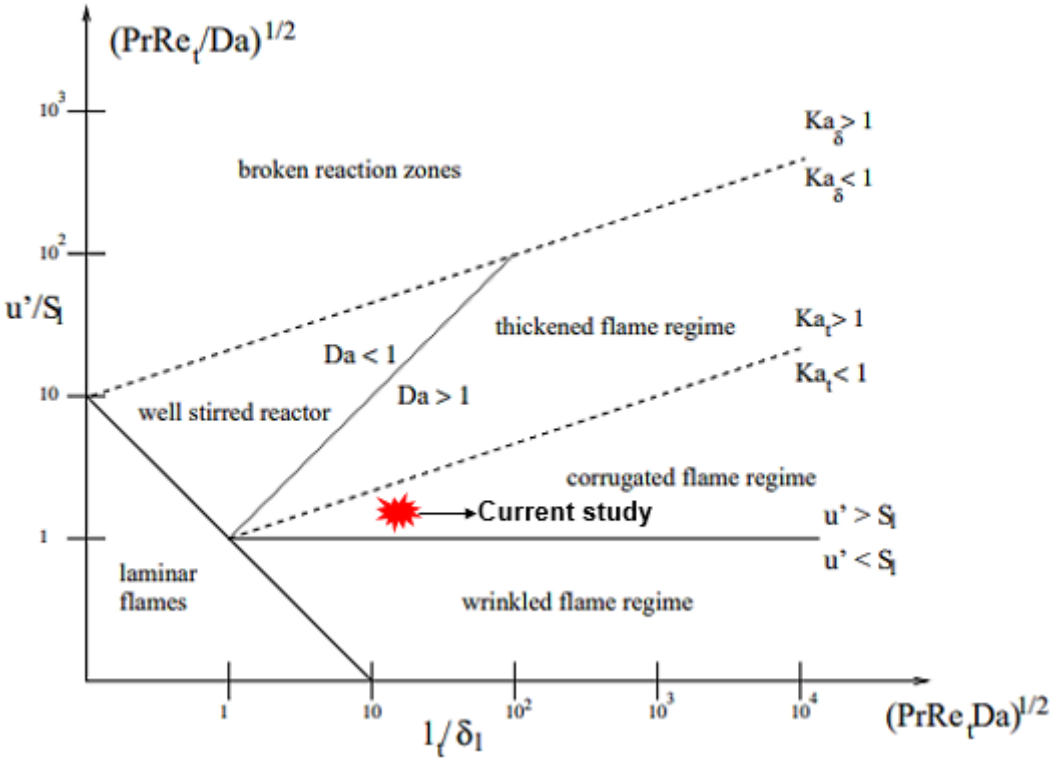

Figure 3.7: Current combustion regime in turbulent premixed combusiton diagram

3.5 Validation

Current numerical model is validated with the experiments and LES. Figure 3.8 shows the validation of the turbulence model with experiments done by Sabatino et al. and LES done by Maestro et al and figure 3.9 shows the validation of turbulence-combustion mode with the experiments done by Palies et al. Axial and tangential velocities are obtained at $y/d = 0.2\overline{2}$. L2 norm of the normalized axial and tangential velocities are used for calculating the relative error. Table 3.5 provides the relative errors between the models. The numerical model has a good agreement with the experiments and LES. For both turbulence and turbulence-combustion model, the maximum relative error is very small, except in the case of tangential velocity of the non-reacting flow from PIV. The error is very high when compared to LES.

	Comparison	V_y/V_{in}	V_z/V_{in}
Relative error in non-reacting flow	RANS to PIV	0.0839	0.184
	RANS to LES	0.0719	0.0746
Relative error in reacting flow	RANS to LDV	0.0845	0.0798

Table 3.5: Relative errors in V_y/V_{in} and V_z/V_{in} between the current model, LES and experiments

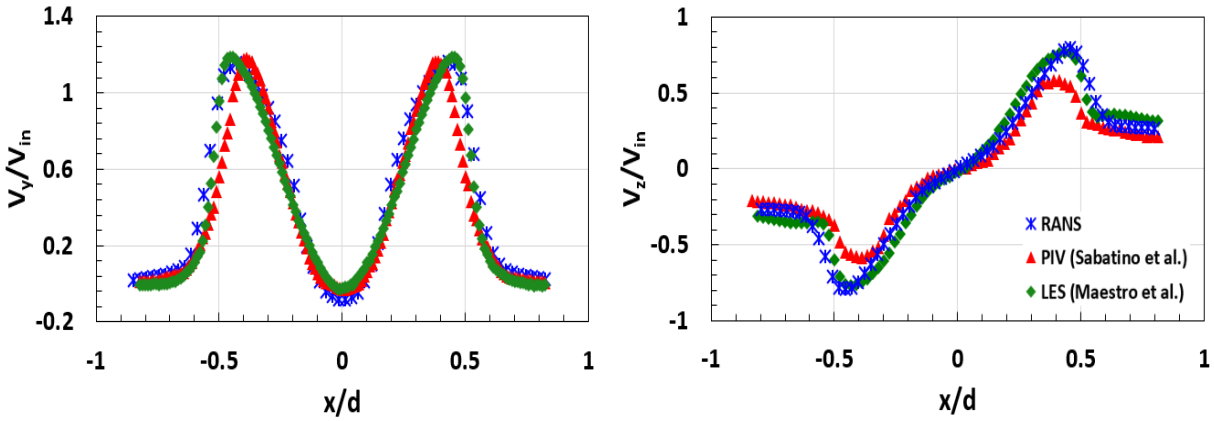

(a) Axial velocity **(b)** Tangential velocity

Figure 3.8: Comparison of velocity profiles, at $y/d = 0.2\overline{2}$, between RANS, LES and PIV in non-reacting flow

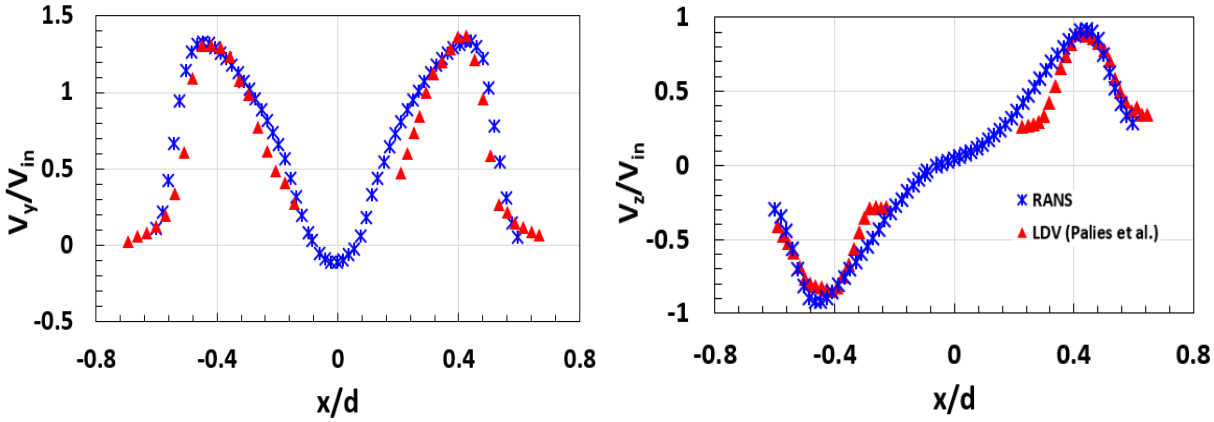

(a) Axial velocity **(b)** Tangential velocity

Figure 3.9: Comparison of velocity profiles, at y/d = 0.15, between RANS and LDV in reacting flow

Chapter 4

Results and Discussion

The computational results are presented and discussed in this chapter. The results include effects of blade angle and central rod in non-reacting and reacting flows.

4.1 Swirl Number

Two types of swirl numbers, flow swirl number and geometrical swirl number, were calculated. The flow swirl number was calculated using equation 2.1, while geometrical swirl number for a radial swirler was calculated using [54],

$$S_G = \frac{1}{1-\Psi} \tan\alpha \frac{R}{2L}\left[1 - \frac{R_C}{R}\right] \tag{4.1}$$

$$\Psi = \frac{zs}{2\pi R} \cos\alpha \tag{4.2}$$

where Ψ is the blockage factor, α is the blade angle, R is the radius of the injection tube, L is the length of the blade span, R_C is the radius of the central rod, z is the number of blades, s is the thickness of the blades.

The following table lists the calculated geometric and flow swirl numbers for the cases with and without a central rod. The flow swirl number was calculated at the exit of the swirler, $y/d = -2.2\overline{7}$.

Blade Angle	**Geometrical Swirl Number**		**Flow Swirl Number**	
Central Rod	**+**	**-**	**+**	**-**
30°	0.68	0.69	0.66	0.63
35°	0.83	0.83	0.77	0.78
37°	0.90	0.90	0.81	0.86
40°	1.02	1.00	1.06	0.96
45°	1.26	1.19	1.38	1.31

Table 4.1: Geometrical and flow swirl numbers at different blade angles

In general, swirl number obtained from the equation 4.1 does not account for the momentum losses and assumes that the tangential velocity is uniform in the radial direction. The geometrical swirl number is slightly higher than the flow swirl number up to 40° blade angle. But, at 45°, the flow swirl number was higher than the geometrical. The over-prediction between the two swirl numbers is less than 10%. This could be because of the realizable $k - \epsilon$ model. At, very high swirl numbers, this model can over-predict the solution. Presence of a cylindrical central rod has very minimal effect on the swirl numbers. Decay in swirl intensity was observed along the downstream direction due to the tangential momentum losses near the walls. Figure 4.1 shows the variation of swirl number in the axial direction for different blade angles in non-reacting and reacting flows for the two cases, with and without a central rod. Swirl numbers are plotted from the exit of the swirler to $0.6d$ downstream of the combustion chamber. The exit of the injection tube is at $y/d = 0$.

Upstream of the combustion chamber, in the injection tube, swirl numbers in non-reacting and reacting flow are almost similar with an average error less than 5% between them. There is an increase in the swirl number as the flow enters the expansion, due to the increase in the flow area. At $y/d = 0.15$, reacting flow experiences a higher swirl number, with a small

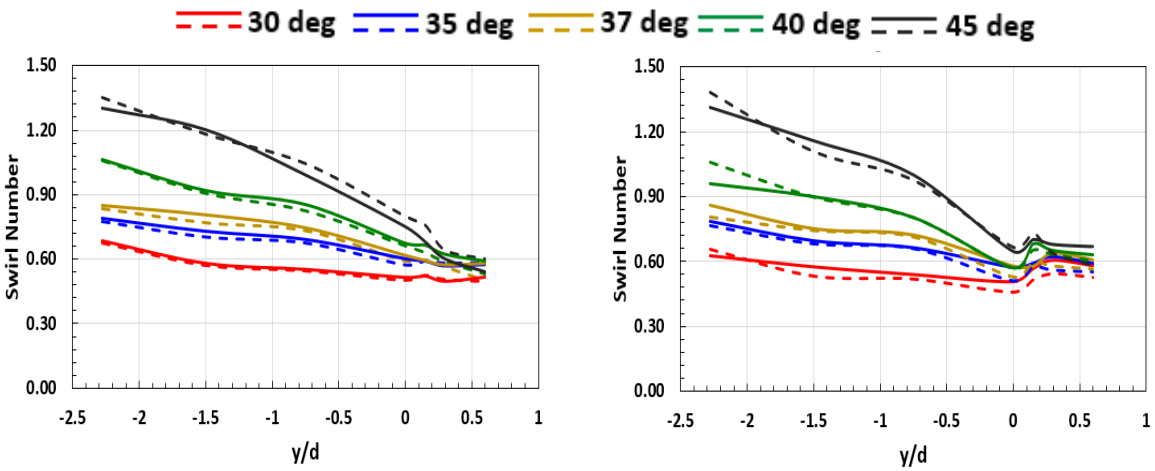

(a) Non-reacting flow **(b)** Reacting flow

Figure 4.1: Swirl number variation along the axial distance for different blade angles in non-reacting and reacting flows. Solid lines - Without central rod and Dashed lines - With central rod

bump, than the non-reacting flow, due to decrease in the density in the reaction zone. This reduction in density is a result of combustion in the reaction zone. From this location, it starts to decrease and almost remains constant in downstream of the combustor. Also, the presence of the central rod has a small influence on the swirl intensity because of the small diameter.

4.2 Axial Velocity

Combustion has a significant effect on the axial velocity. Due to the thermal expansion in a reacting flow, the axial velocities are higher when compared to the reacting flow. Figure 4.2a shows the radial distributions of axial velocity profiles, obtained at $y/d = 0.2\overline{2}$ in non-reacting and reacting flows, with and without a central rod for different swirl numbers.

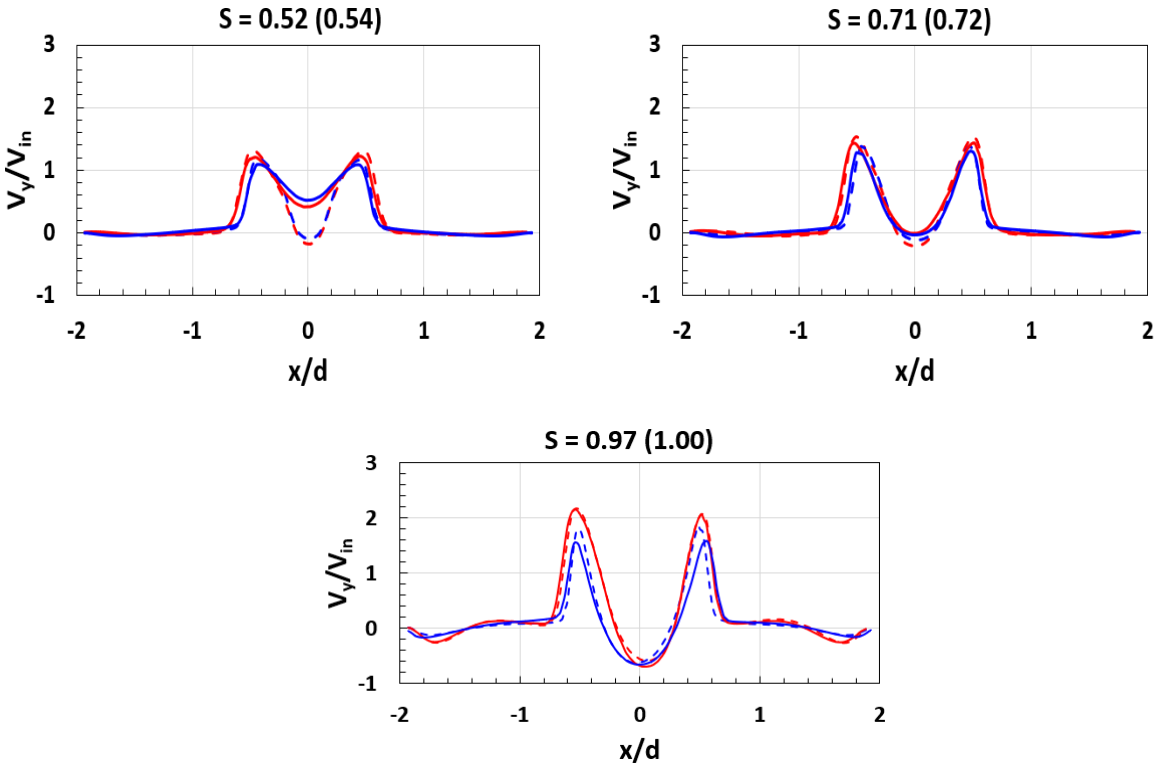

(a) Normalized axial velocity profiles at different swirl numbers

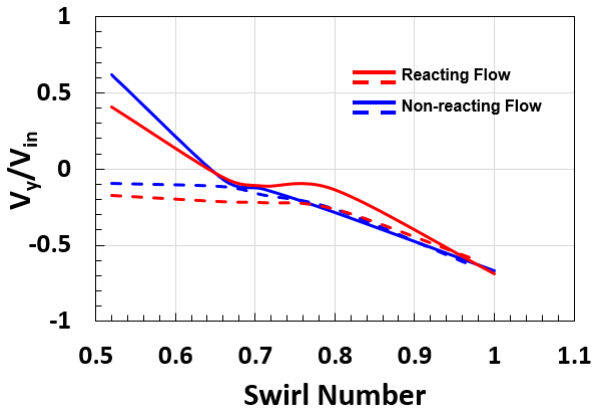

(b) Normalized axial velocity at $x/d = 0$

Figure 4.2: Normalized axial velocity profiles in non-reacting and reacting flows at $y/d = 0.2\overline{2}$ for different swirl numbers. Solid lines - Without Central Rod and Dashed lines - With Central Rod

For the swirl number, $S = 0.54$, the stagnation point (where $V_y/V_{in} = 0$) in the case without a central rod is slightly downstream when compared to the case with the central rod. In the absence of the central rod, flow is stabilized downstream, because of the insufficient swirl. Whereas the central rod stabilizes flow far upstream and its presence moves the stagnation point further upstream, indicating a deeper central toroidal recirculation zone (CTRZ) as observed

by Durox et al.[9]. Figure 4.2b shows the axial velocities at $x/d = 0$. As the swirl number is increased, axial velocity gets more and more negative. At this axial location, $y/d = 0.2\overline{2}$, a significant difference, in non-reacting and reacting flows, is observed for $S = 0.97$. Due to thermal expansion, the reacting flow has a higher axial velocity when compared to the non-reacting flow.

Along the axial direction, width of the recirculation zone, CTRZ, increases. Figure 4.3a and figure 4.3b presents normalized axial velocities in non-reacting and reacting flows, with and without the central rod for different swirl numbers, respectively. Bulk velocity (V_{in} = 6.45 m/s) at the exit of the injection tube is used for normalization. Axial velocities in reacting flow have a larger magnitude when compared to the non-reacting flow due to the thermal expansion. From $y/d = 0.6$ to $y/d = 3.0$, width of the CTRZ increases, and the corner recirculation zone (CRZ) disappears due to flow reattachment at the chamber walls.

Figure 4.4 shows the contours of axial velocity in $xy - plane$, mid-plane of the combustion chamber.The left half in the figure 4.4 represents reacting flow, while the right half represents non-reacting flow with black solid lines indicating the zero velocity lines. The top row showcases the case with central rod and bottom row corresponds to the case without central rod.

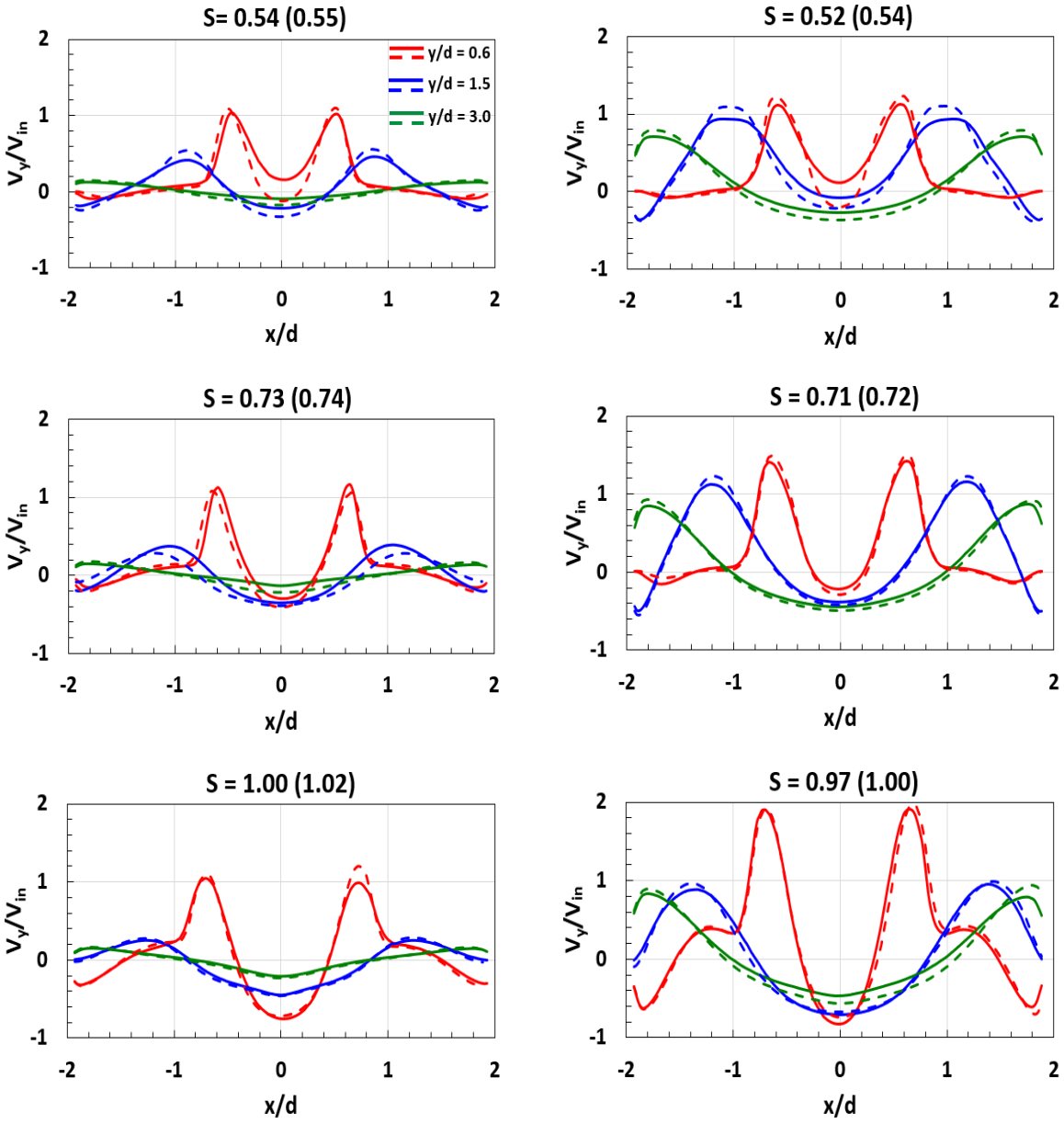

(a) Non-reacting flow (S in parentheses is without central rod)

(b) Reacting flow (S in parentheses is without central rod)

Figure 4.3: Normalized axial velocity profiles of non-reacting and reacting flows, with and without the central rod at different axial locations: Solid lines - Without Central Rod and Dashed lines - With Central Rod

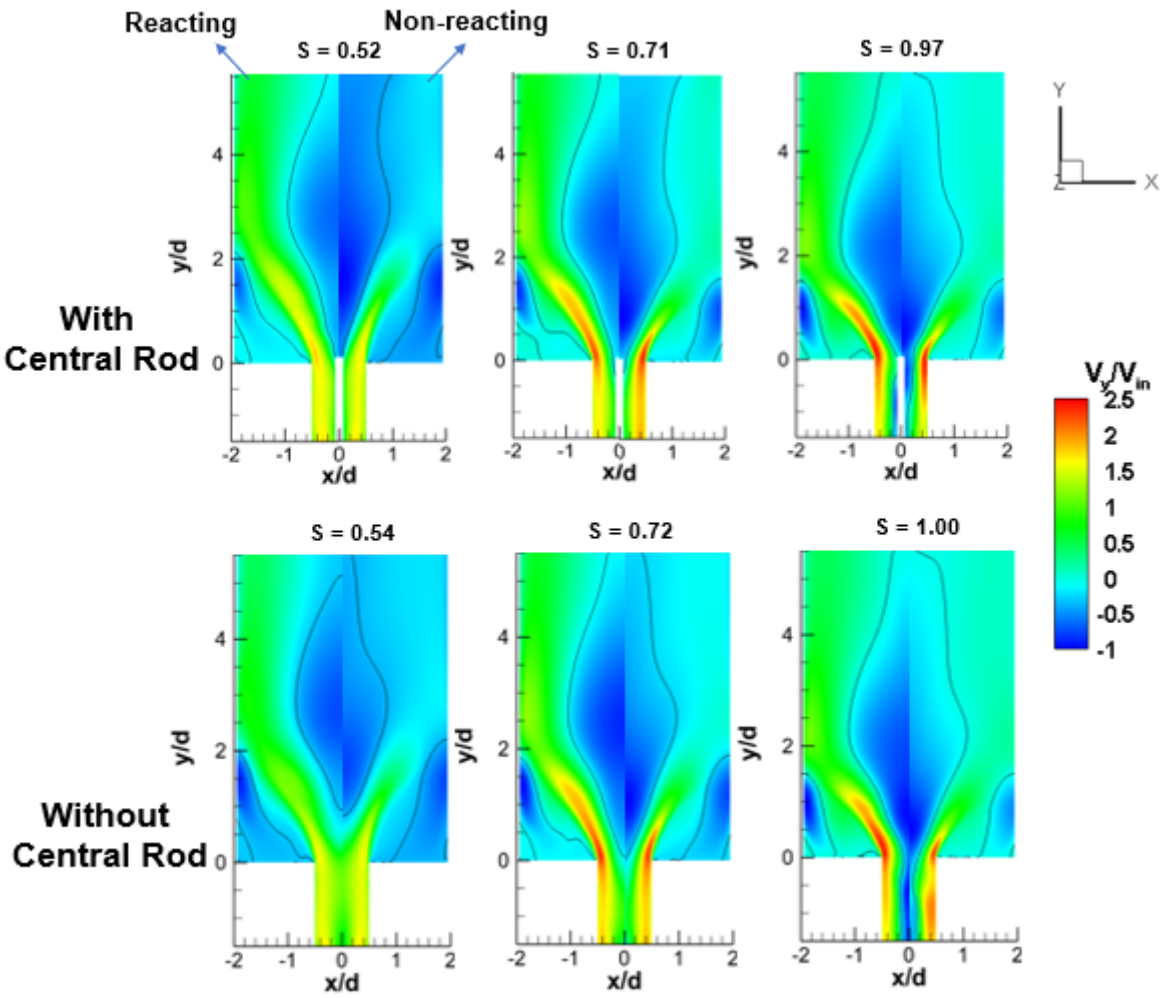

Figure 4.4: Normalized axial velocity contours of non-reacting and reacting flows, with and without the central rod in the mid-plane (xy-plane): Solid black lines indicate the zero velocity line

At $S = 0.52$, the CRZ, as a result of sudden expansion, extends up to $2d$ downstream of the combustion chamber, as the flow reattaches to the wall at this point after the expansion. This is because, the flow moves slowly towards the wall at a low swirl numbers. As the swirl is increased, the flow moves faster towards the chamber wall and also the flow reattachment point moves upstream. This considerably reduces the size of the CRZ. The CTRZ acts a solid body, around which the flow is stabilized.

Due to the thermal expansion of gases, the axial velocity in reacting flow along the wall is higher than the non-reacting flow. The width of the CTRZ increases with increase in the swirl number. Reacting flow exhibits slightly wider CTRZ than the non-reacting flow. As

the swirl number goes beyond the critical swirl number (here, $S > 0.7$), the adverse pressure gradient $\frac{\partial p}{\partial y}$ in the axial direction, applies a force on the upstream flow and makes the CTRZ move upstream as predicted by Mansouri et al. [7] and their results are shown in figure 1.2. At low swirl numbers, the central rod helped the flow to stabilize near the exit of the injection tube by decreasing the flow velocity around the rod. In the absence of this central rod, at low swirl numbers, the CTRZ is stationed at 1d downstream of the injection tube. At higher swirl numbers, both the cases, with and without the central rod exhibit similar flow behavior.

Figure 4.5 shows the axial velocity contours in $xz - plane$ in non-reacting flow, the bottom half, and reacting flow being the top half. The top row of the figure represents the case with the central rod and the bottom row corresponds to the case without the central rod.

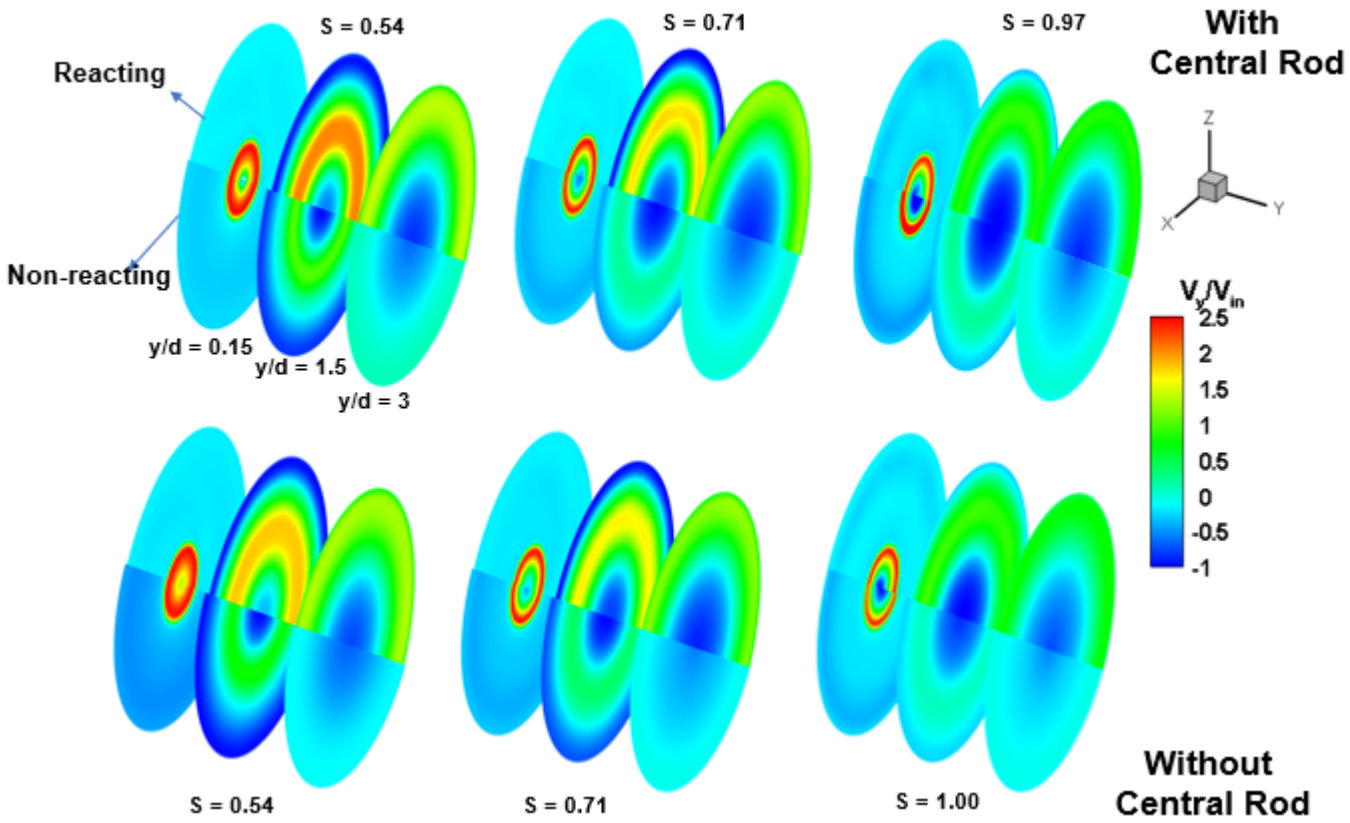

Figure 4.5: Normalized axial velocity contours in xz-plane of non-reacting and reacting flows, with and without the central rod at different axial locations

The planes are extracted at three axial locations, $y/d = 0.15$, 1.5 and 3.0. As the flow

transitions in axial direction, the CRZ slowly disappears. Presence of rod has very minimal effect on the downstream flow. Also, the maximum velocity is observed for reacting flow in the shear layers, when compared to the non-reacting flow.

4.3 Tangential Velocity

Tangential velocity depends on the swirl number in swirl flows. Figure 4.6a shows the normalized tangential velocities at $y/d = 0.2\overline{2}$ in non-reacting and reacting flows with and without the central rod for different swirl numbers. As the swirl number is increased from 0.52(0.54) to 0.97(1.00) tangential velocity also increased in all the four cases. But, it almost remains same even in the presence of flame. In reacting flow case, cannot expand in a prescribed tangential direction because of the symmetry. So, tangential velocity is hardly affected by the flame. Central rod has a very minimal effect on tangential velocity, because the tangential velocity acts away from the center. Maximum tangential velocity is observed at the edge of the CTRZ and the flow in the central region resembles to a solid body rotation.

Figure 4.6b represents the normalized maximum tangential velocities for different swirl numbers. Maximum tangential velocity increases with increase in the swirl number as mentioned earlier. Tangential velocity decays along the downstream direction due to viscous effects and a reduction in the centrifugal force generated by the swirl. Figure 4.7 shows the normalized tangential velocity profiles at three axial locations $y/d = 0.6, 1.5$ and 3.0. Increase in the swirl number resulted in increase of the tangential velocity. But, the velocity profiles get flatter as the flow moves downstream.

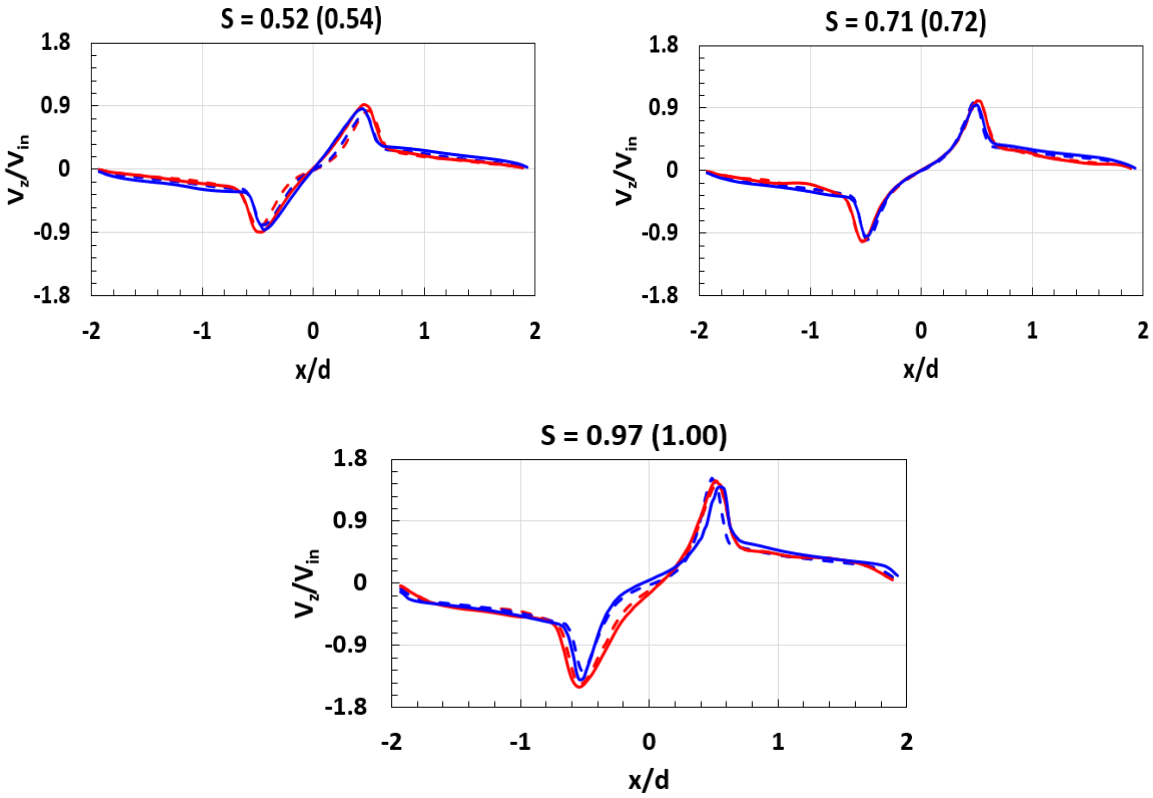

(a) Normalized tangential velocity profiles at different swirl numbers

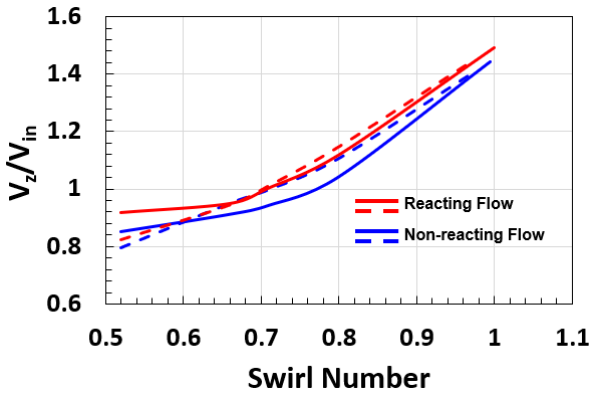

(b) Normalized maximum tangential velocity at $x/d = 0$

Figure 4.6: Normalized tangential velocity profiles in non-reacting and reacting flows at $y/d = 0.2\overline{2}$ for different swirl numbers. Solid lines - Without Central Rod and Dashed lines - With Central Rod

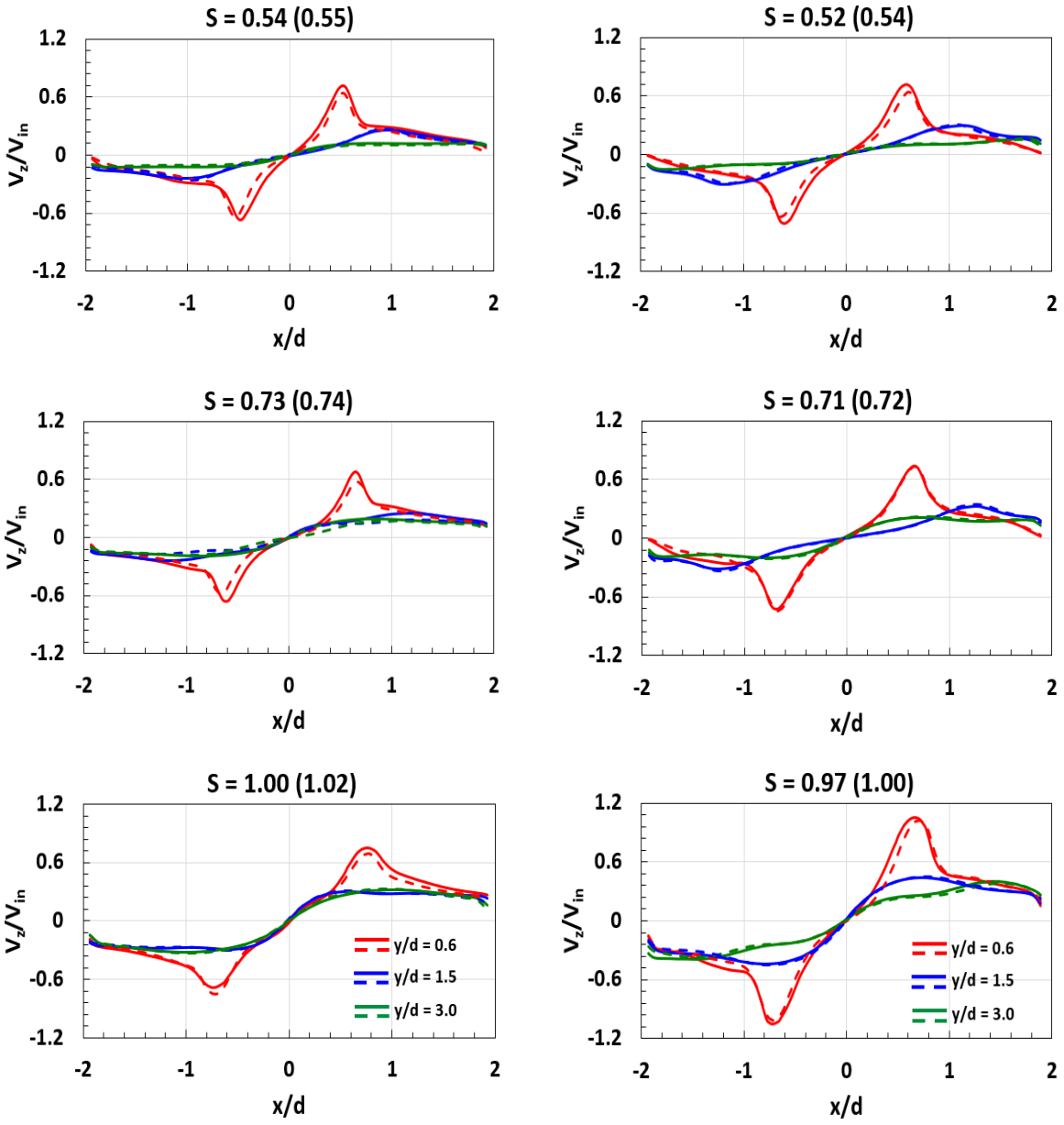

(a) Non-reacting flow (S in parentheses is without central rod)

(b) Reacting flow (S in parentheses is without central rod)

Figure 4.7: Normalized tangential velocity profiles of non-reacting and reacting flows, with and without the central rod at different axial locations: Solid lines - Without Central Rod and Dashed lines - With Central Rod

4.4 Turbulent Kinetic Energy

A very high turbulent kinetic energy (TKE) is observed in downstream regions of the centerbody and the injection tube exit. In the inner shear layer between the incoming flow and

CTRZ, large velocity fluctuations are observed due to the turbulent mixing and this matches with the results from the experiments of Park et al.[37]. Figure 4.8 shows the normalized TKE contours in non-reacting and reacting flows with and without central rod for different swirl numbers. Maximum TKE ($TKE_{max} = 39.6 m^2/s^2$) is used for normalization.

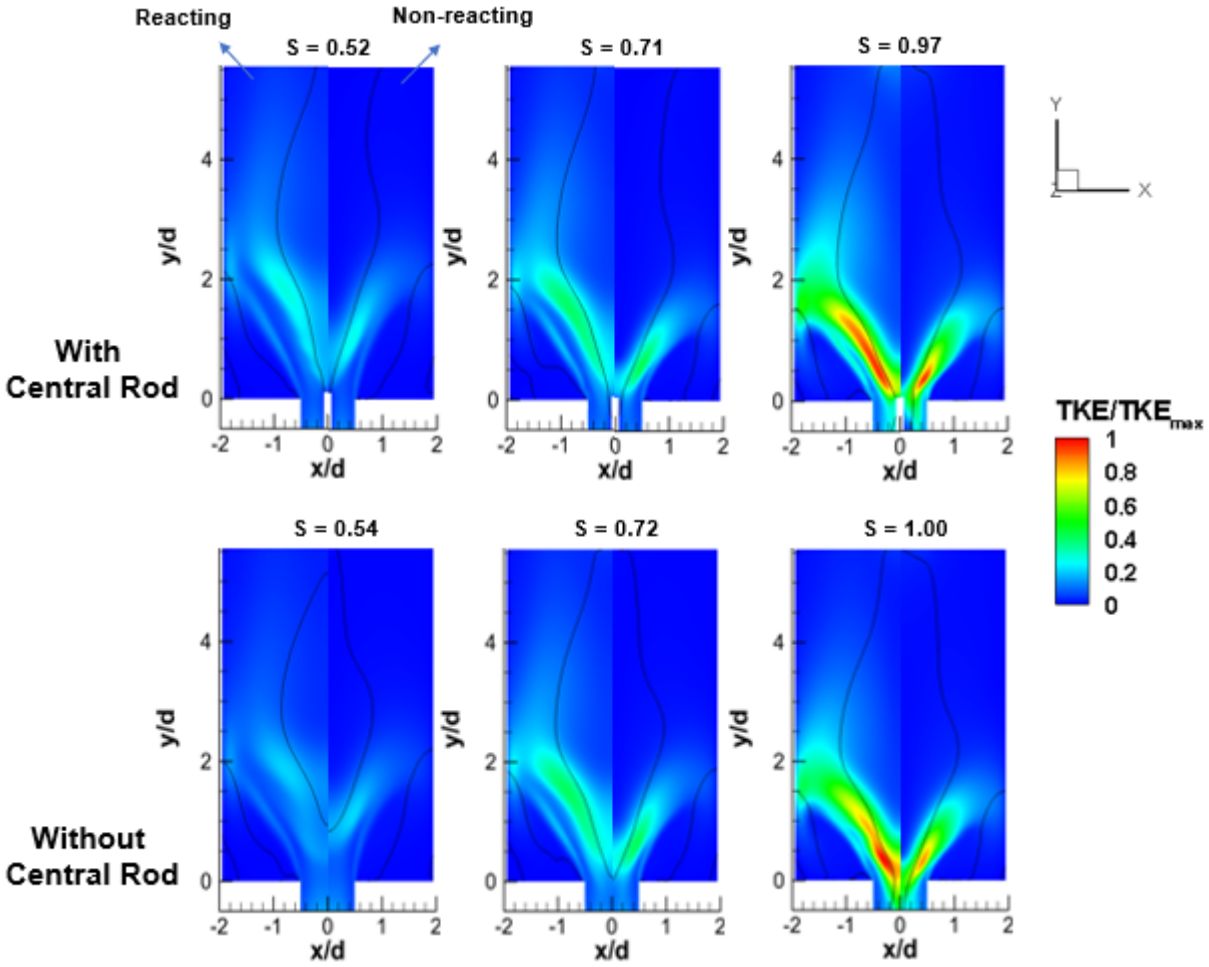

Figure 4.8: Turbulent kinetic energy contours on the mid-plane (xy-plane) for non-reacting and reacting flows, with and without the central rod: Solid lines indicate the zero velocity lines

The left half of the contour represents reacting flow and the right half of the contour corresponds to the non-reacting flow. The top row represents the case with the central rod and bottom row represents the case without the central rod. TKE observed in the shear layers of the reacting flow is higher than the non-reacting flow. The shear layers in non-reacting flow are shorter when compared to the reacting case. This is because of the thermal expansion of gases from combustion. With an increase in the swirl number, the turbulent intensity is increased due

to rapid mixing and it is very high at $S = 0.97(1.00)$. For the case without the central rod at $S = 0.54$ yields a lower turbulent region in the inner shear layers, when compared to the case with a central rod. This is due to the reduced interaction between the CTRZ, which is stationed a little far from the injection tube exit, and inflow. Figure 4.9 shows the distribution of maximum TKE in the inner shear layers for different swirl numbers in non-reacting and reacting flows. The maximum TKE was obtained on the axial planes from the exit of the injection tube till 2.5d downstream and the maximum value is observed in inner shear layers.

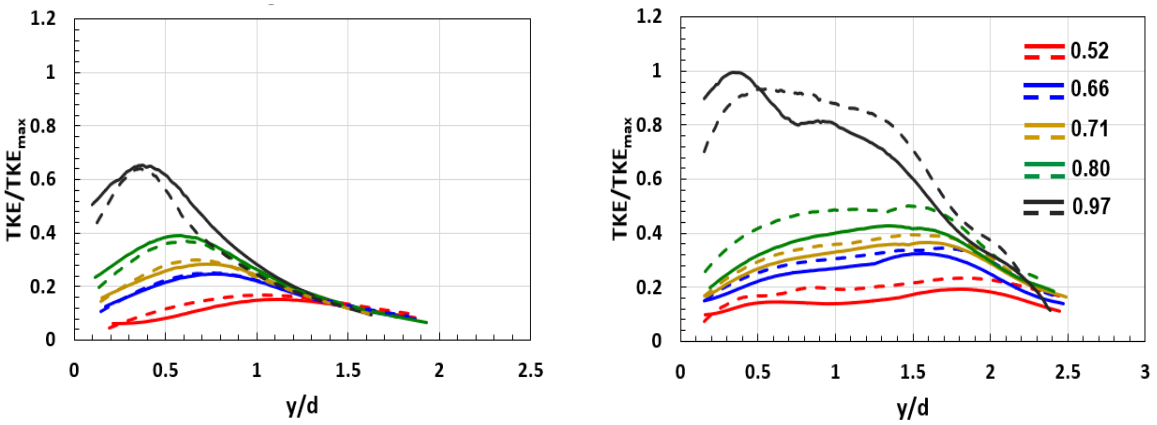

(a) Non-reacting flow **(b)** Reacting flow

Figure 4.9: Normalized maximum turbulent kinetic energy profiles on the axial planes in non-reacting and reacting flows, with and without the central rod for different swirl numbers: Solid lines - Without Central Rod and Dashed lines - With Central Rod

The maximum TKE shifts to left, moves towards the injection tube, because the CTRZ moves upstream and the interaction between the inner shear layer and CTRZ gets closer to the injection tube. Both the cases with and without the central rod in non-reacting flow almost have the same TKE distribution. But, in reacting flow, especially for $S = 0.8, 0.97$ the TKE distribution varies because, the CTRZ moves upstream and encloses the shear layer in the case with central rod.

4.5 Temperature

Swirl number has a major effect on the flame temperature and combustion. High swirl number provides a very good mixing of incoming reactants, and this rapid mixing decreases the length of the flame. For flame stabilization, the flame speed should match the speed of the incoming reactants. Figure 4.10 normalized temperature contours in mid plane of the combustion chamber for the case with and without the central rod. Inlet temperature ($T_0 = 300K$) was used for the normalization.

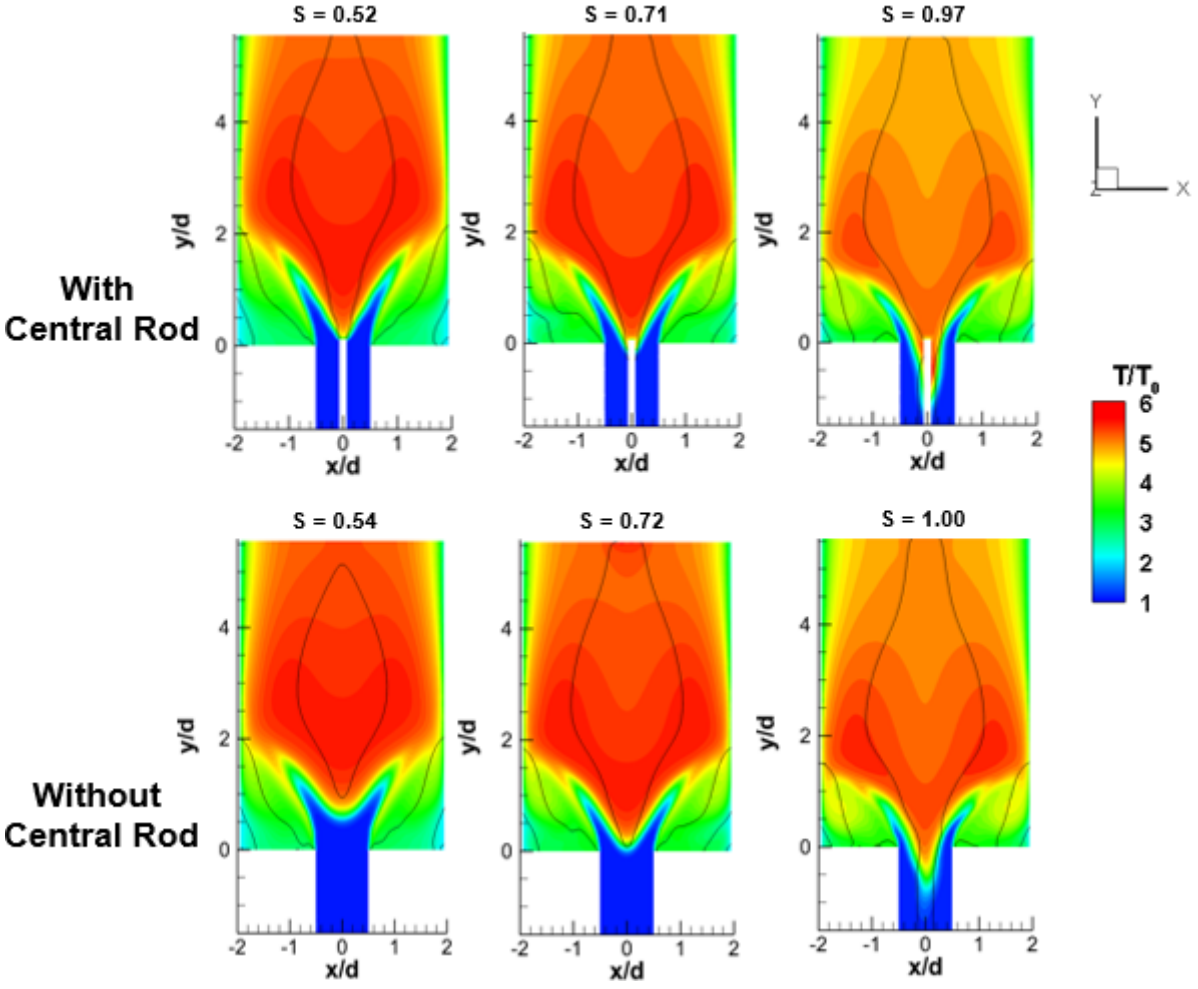

Figure 4.10: Temperature contours on the mid-plane (xy-plane) for non-reacting and reacting flows, with and without the central rod: Solid lines indicate the zero velocity lines

At low swirl in the case with the central rod, $S = 0.52(0.54)$, the flame is stabilized on top of the rod. But, in the case without the central rod, the flame is stabilized aerodynamically

at a distance from the injection tube exit. As the swirl number is increased from $S = 0.52(0.54)$ to$S = 0.97(1.00)$, the flame length is reduced. Also, the flame starts to move upstream, creating a flashback as predicted by Mansouri et al. [7]. This is shown in the figure 1.3 The case with the central rod exhibits higher flashback than the case without the central rod at very high swirl number, $S > 0.9$. This is because of the boundary layer developed near the rod. This is observed by Ebi et al. [55] and Nauert et al. [56] in their studies. The maximum flame temperature observed for $S = 0.52(0.54)$ is close to $6T_0$ and it reaches $5.5T_0$ for $S = 0.97(1.00)$. The width of the CTRZ increases with increase in the swirl number. As a result of this increase in the width, CTRZ entrains more fresh reactants near the injection tube exit which raises the heat loss from the reaction zone, thereby reducing the flame temperature. The CRZs have lower temperatures when compared to the other regions in the combustion chamber, because of the heat loss to the chamber walls and the lean mixture of reactants that is trapped due to sudden expansion.

Figure 4.11 presents the normalized temperature profiles along the centerline of the combustion chamber for the cases with and with the central rod. The injection tube exit is at $y/d = 0$.

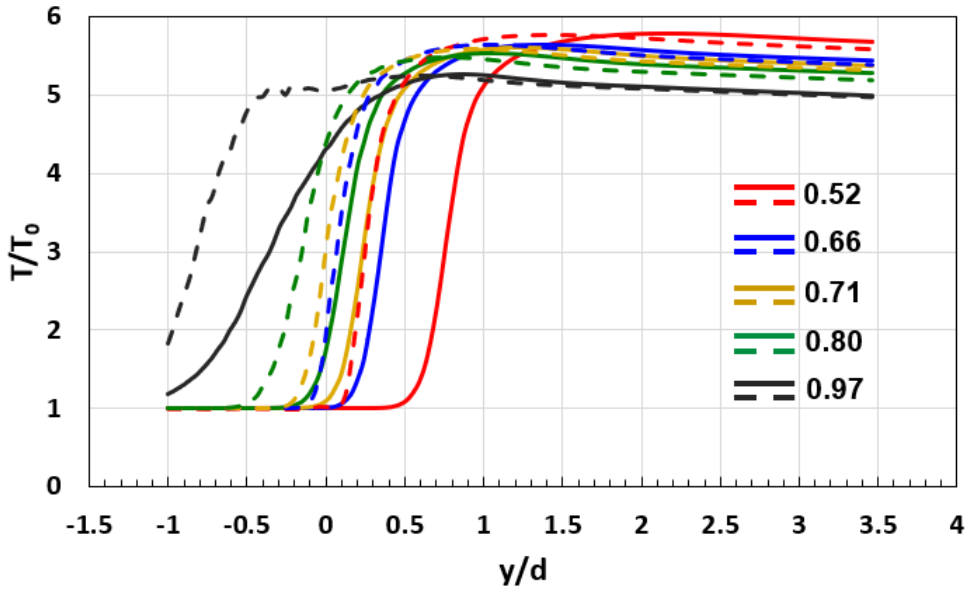

Figure 4.11: Normalized temperature profiles along the centerline of non-reacting and reacting flows, with and without the central rod for different swirl numbers: Solid lines - Without Central Rod and Dashed lines - With Central Rod

As the swirl number is increased, the flame starts to flashback and the temperature along the centerline decreases. This is because of the excess turbulence created by the high swirl, which increases the flame speed due to the higher transportation rate of species. This flame speed is higher than the speed of the incoming reactants. Both the cases, with and without the central rod are same, with a very small difference, after they reach the maximum flame temperature. This is in good agreement with the Ouali et al.'s [8] work and the temperature distribution is shown in figure 1.4.

4.6 Species Mass Fractions

Mass fractions of the species are shown in the figure 4.12 for different swirl numbers with and without the central rod.

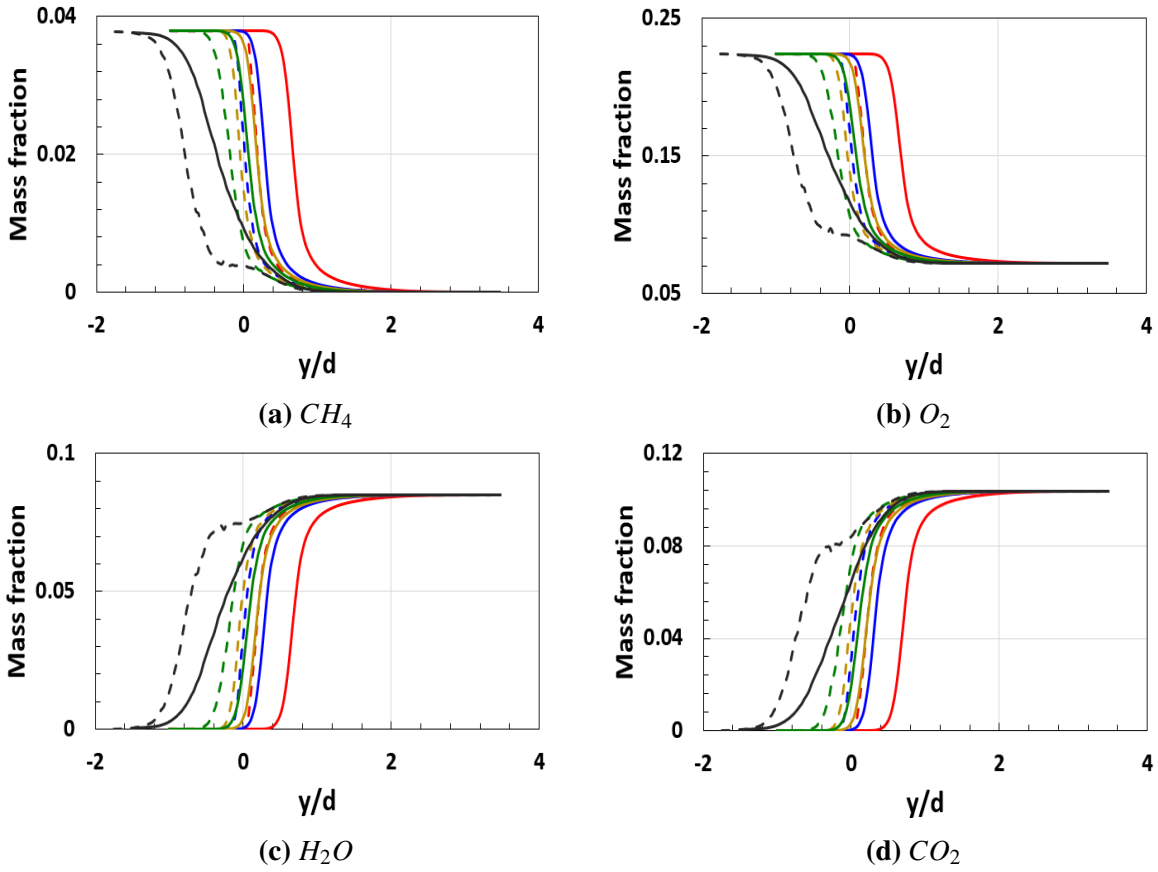

(a) CH_4 **(b)** O_2

(c) H_2O **(d)** CO_2

Figure 4.12: Species mass fractions along the centerline of the combustion chamber: Solid lines - Without Central Rod and Dashed lines - With Central Rod

Swirl number has a significant effect on the product formation. At higher swirl numbers, $S = 0.8(0.82), 0.97(1.00)$, product formations start in the injection tube, indicating a flashback. Mass fraction of CH_4 decreases along the downstream direction and almost reaches zero in the combustion chamber indicating complete combustion. Similarly, mass fraction of O_2 also decreases in downstream direction, but, reaches a minimum value, as the reaction is lean. Mass fractions of H_2O and CO_2 indicate progress of the reaction and they increase with axial distance and remain constant from $y/d = 1.9$. At this axial location, the reaction is complete. Figure 4.13 shows the mass fractions of some of the key species in the methane-air premixed combustion. Since CO is an intermediate product, it's formation starts as soon as the reaction is initiated and disappears before the reaction is complete. High mass fraction of is observed

in the low temperature region. As soon as the temperature gets higher, the mass fraction of CO starts to decrease. This is due to the oxidation of CO which occurs at high temperatures as predicted by Nguyen et al.[57]. It is observed that the rate of reaction in the case of the central rod is faster, compared to the case without the central rod.

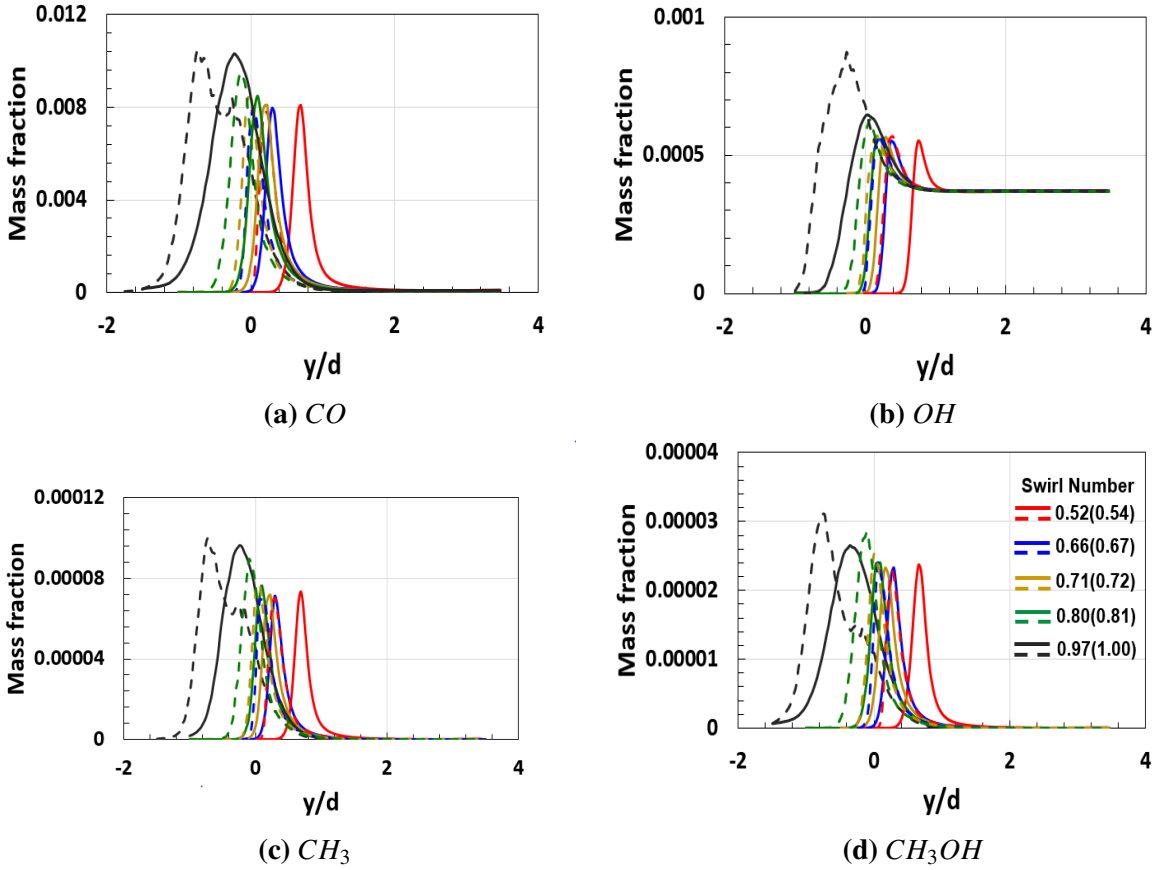

(a) CO **(b)** OH

(c) CH_3 **(d)** CH_3OH

Figure 4.13: Mass fractions of key species along the centerline of the combustion chamber: Solid lines - Without Central Rod and Dashed lines - With Central Rod

Figure 4.13b shows the mass fraction of OH along the centerline of the combustion chamber. The mass fraction of OH increases sharply and attains a maximum value in the reaction zone. Once it reaches the maximum value, it starts to decrease and will reach equilibrium in the downstream of the reaction zone, through a series of recombination reactions with the other species. The sharp gradient that is observed in the reaction zone corresponds to the edge of the flame as predicted by Strakey et al. [58], and this indicates the location of the flamefront.

At low swirl number, the flame in the case without the central rod is located 0.8d downstream. As the swirl number is increased, the peak OH value moves upstream indicating the movement of the flame upstream. The location of the peak values of OH in case with the central rod is more upstream because of the higher flash back. Higher mass fractions of CH_3 corresponds to the slower flame propagation as observed by Li et al. [59]. At high swirl numbers, the mass fraction increases contributing to the lower flame speed. CH_3OH is formed due to the recombination reactions between CH_3 and OH radicals. Production and formation of CH_3OH is completed well within the reaction zone. For swirl numbers greater than 0.6, the species formation starts way upstream in the both the cases with and without central rod. The species mass fraction increases with increasing swirl number, and the peak value moves upstream of the injection tube.

4.7 NO_x Emissions

Thermal NO_x emissions are studied for different swirl numbers including the effects of the central rod. Figure 4.14 shows the variation of NO_x emissions with normalized flame temperature and swirl number at the exit of the combustion chamber. Thermal NO_x have strong affinity to high temperatures. So, they are formed at these high temperatures due to the oxidation of nitrogen. The concentration of thermal NO_x decreases with increase in the swirl number. This is because of the decrease in the flame temperature, which reduces the NO_x concentrations. The case without the central rod shows higher NO_x concentration than the case with the central rod at S = 0.52. This is due to the flame stabilization that happens farther downstream of the combustion chamber, and this stabilization increases the temperature near the exit of the combustion chamber. The results are in good agreement with the literature [10].

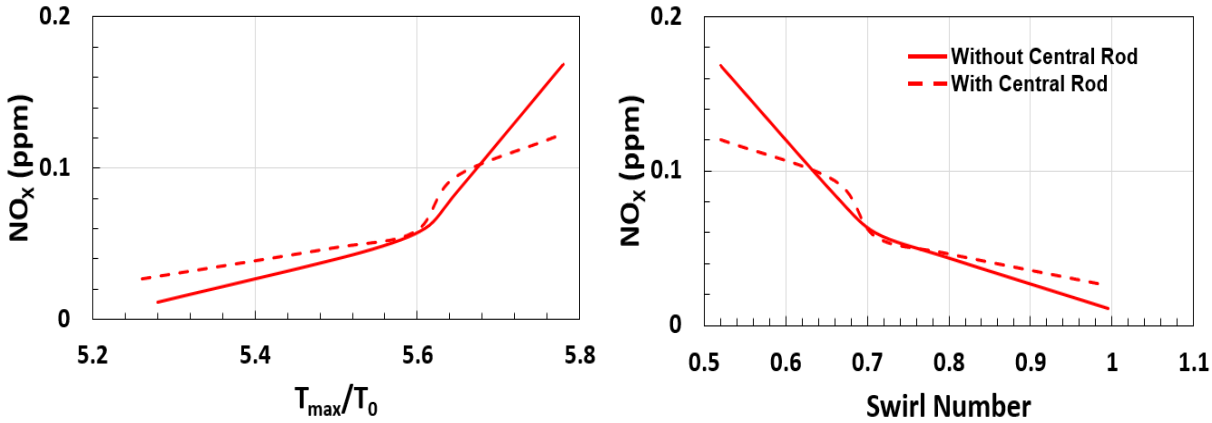

(a) NO_x (ppm) vs Normalized flame temperature

(b) NO_x (ppm) vs Swirl number

Figure 4.14: Variation of NO_x emissions with flame temperature and swirl number at the outlet

Figure 4.15 shows the NO_x distribution along the centerline of the combustion chamber for different swirl numbers. The NO_x concentration increases till 2d in the combustion chamber due to the presence of flame and hot recirculating gases. It starts to decrease after the high temperature region because of the rapid mixing of the combustion products with the excess air in the downstream of the combustion chamber. The case without the central rod produces higher NO_x in the swirl number range, 0.54 to 0.7. This is because of the flame stabilization that is observed a little downstream of the injection tube exit. As the swirl number increases the thermal NO_x concentration decreases along with the difference between the NO_x formation in the two cases, as observed by Ouali et al. [8]. Especially, at high swirl numbers, the concentration is reduced to less than 0.04 ppm, and the case without the central rod produces 0.02 ppm. At high swirl number, S = 0.97(1.00), the case with and without the central rod, small traces of NO_x are formed in the injection tube due to the flashback.

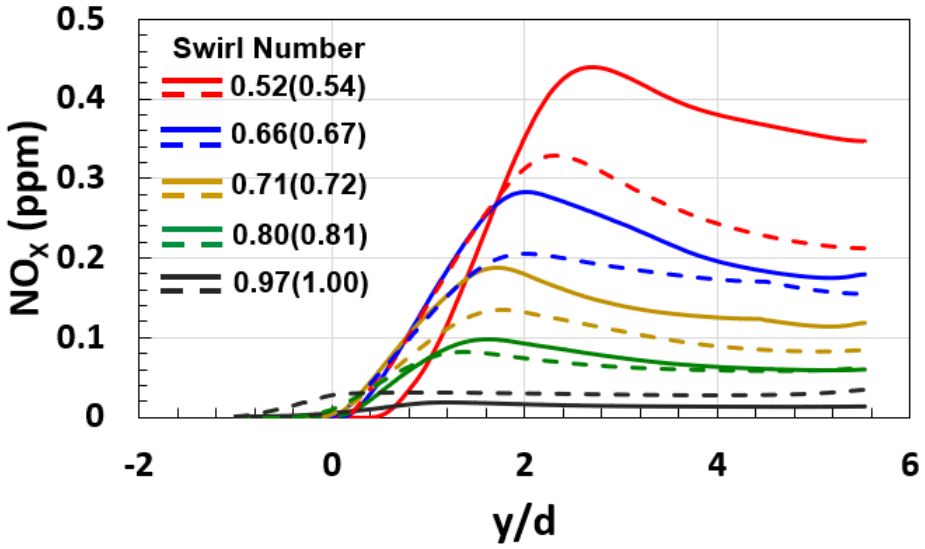

Figure 4.15: NO_x distribution along the centerline for different swirl numbers. Solid lines - Without central rod and Dashed lines - With central rod

The NO_x concentrations are higher in the high temperature regions. Figure 4.16 shows the radial distribution of NO_x concentrations obatained at different sections,y/d = 0.6, 1.5, 3 and 5, in the cases with and without the central rod. High NO_x production is seen in the central toroidal recirculation zone, which is a source for high temperatures. In the downstream direction, especially, near the exit of the combustion chamber, the concentration decreases because of the decay in temperature as a result of the rapid mixing of hot gases with the excess air in the chamber. This is in good agreement with the experimental works of Takagi et al. [11]. At low swirl number, the case without the central rod, especially at y/d = 3.0 and 5.0, produce higher NO_x. As the swirl number increases, the NO_x concentration decreases and the case without the central rod produces very small amounts of NO_x when compared to the case with the central rod.

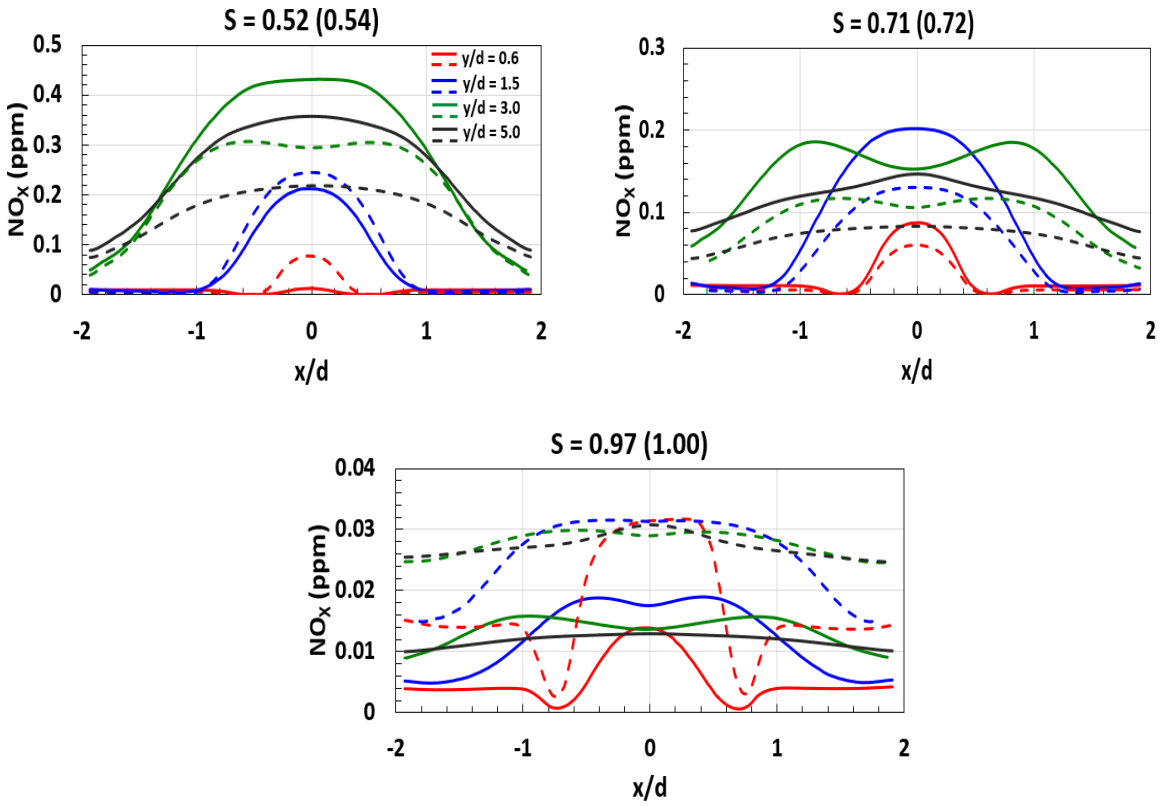

Figure 4.16: NO_x concentrations for different swirl numbers at axial locations, y/d = 0.6, 1.5, 3.0 and 5.0. Solid lines - Without Central Rod and Dashed lines - With Central Rod

Chapter 5

Conclusion and Future Work

5.1 Conclusion

The flow behavior of non-reacting and reacting flow in a lean premixed swirl combustor, adapted from KAUST experimental rig, was studied by RANS using the commercial software, Ansys - Fluent. Turbulence was modeled using the two equation realizable $k - \epsilon$ model and the turbulence - chemistry interaction is modeled by a flamelet generated manifold technique. The simulation results were in good agreement with the experiments and LES. Based on these results, analyses are conducted to study the effect of swirl number and a cylindrical rod on the non-reacting and reacting flows. At first, non-reacting flow was simulated in lean premixed swirl combustor. These simulation results were compared to the experiments done by Sabatino et al.[2] and LES work of Maestro et al.[3]. This non-reacting flow solution was used as an initial condition to the reacting flow for a faster convergence of the solution, with methane-air mixture at an equivalence ratio of 0.67. GRI 3.0 mechanism was used for modeling chemistry, which had 325 chemical equations and 53 species to solve. The reacting flow results were compared with the experiments of Palies et al [4].

Higher axial velocities were observed in reacting flow, when compared to the non-reacting flow, because of the thermal expansion of the gases. Flow reattachment point to the combustion chamber wall after the expansion was moved upstream at high swirl numbers, due to the high centrifugal force, which made the flow move faster towards the wall. A central toroidal recirculation zone (CTRZ) was observed from a swirl number, S = 0.52 in the case with a central rod, and from S = 0.54 in the case without a central rod. This was because of the adverse pressure gradient created at a critical swirl number. This pressure gradient made the flow to reverse, forming a recirculation zone in the combustion chamber. This CTRZ helped to stabilize the flame. At low swirl numbers, the central rod, which was in the injection tube, helped the flow and flame to stabilize on top of it. In the absence of this central rod, the flame is lifted off and stabilized at a distance from the burner exit. Also, the flame length was shortened at high swirl numbers, because of the rapid mixing of fuel air mixture. As the swirl number was increased, the CTRZ started move upstream because of the force, created by the adverse pressure gradient, was acting in negative flow direction. This phenomenon with flame flashback was observed from S = 0.7. A very high turbulence was observed in the inner shear layer because of the turbulent interaction between the flow in these shear layers and the recirculation zone. At high swirl numbers, as the CTRZ moved upstream, the turbulent kinetic energy was very high near the burner exit and the in shear layers. This was due to the CTRZ encased the inner shear layer, causing a high turbulent interaction. Central rod is best suited at low swirl numbers. Whereas, at high swirl numbers (S>0.6), the need for the central rod was minimized.

NO_x emissions were higher in the regions of high temperature. Along the downstream direction, the NO_x concentration was increased. But, it started to decrease near the exit of the combustion chamber due to the decrease in the temperature. CTRZ was a source of high

temperatures. Due to this, higher NO_x was observed in CTRZ. The NO_x concentrations were decreased with increasing swirl numbers. The case without the central rod produced slightly lower NO_x, when compared to the case with the central rod. This was because of the lower temperatures observed in the case without the central rod.

5.2 Future Work

The current study was focused on the effect of geometrical parameters and did not consider pollutant emissions. All the simulations for the current study were performed in steady state to study the flow behavior. Transient simulations will provide more information about the combustion dynamics. It will be interesting to study how the heat release rate fluctuates in response to the inlet velocity changes, which is explained in terms of a flame transfer function. Future work will include the study of this flame transfer function and pollutant emissions. Also, it will focus on the behavior of the flame under external excitations and the thermo-acoustics associated with it.

Bibliography

[1] R T Robert, W Changlie, and C Kyung. Low nox lean direct wall injection combustion concept. 2003.

[2] F D Sabatino, D A Lacoste, and W L Roberts. A detailed characterization of a high pressure experimental apparatus for flame dynamic studies. pages 1–6, 2017.

[3] D Maestro and D Lacoste. Large Eddy Simulation of Nanosecond Repetitively Pulsed Discharges for the Control of Thermoacoustic Instabilities. 33(0):1–12.

[4] P Palies, D Durox, S Schuller, and S Candal. Experimental study on the effect of swirler geometry and swirl number on flame describing functions. *Combustion Science and Technology*, 183.

[5] L Durand. Development, implementation and validation of les models for inhomogeneously premixed turbulent combustion, 2007.

[6] Y Huang and Yang V. Swirling flow structures and flame characteristics in a leanâĂŞpremixed combustor. *42th AIAA Aerospace Sciences Meeting and Exhibit*, 2004.

[7] Z M Mansouri, M Aouissi, and T B Boushaki. A numerical study of swirl effects on the flow and flame dynamics in a lean premixed combustor. *International Journal of Heat and Technology*, 34(2), 2016.

[8] S Ouali, A H Bentebbiche, and T Belmrabet. Numerical Simulation of Swirl and Methane Equivalence Ratio Effects on Premixed Turbulent Flames and NOx Apparitions. 9(2):987–998, 2016.

[9] D Durox, J P Moeck, J Fçois Bourgouin, P Morenton, M Viallon, T Schuller, and S Candel. Flame dynamics of a variable swirl number system and instability control. *Combustion and Flame*, 160(9):1729–1742, 2013.

[10] A. M. Elkady, J. Herbon, D. M. Kalitan, G. Leonard, R. Akula, H. Karim, and M. Hadley. Gas Turbine Emission Characteristics in Perfectly Premixed Combustion. *Journal of Engineering for Gas Turbines and Power*, 134(6):061501, 2012.

[11] T Takagi and T Okamoto. Characteristics of combustion and pollutant formation in swirling flames. *Combustion and Flame*, 43:69–79, 1981.

[12] A K Gupta, D G Lilley, and N Syred. *Swirl Flows*. Abacus Press.

[13] T Sarpkaya. On stationary and traveling vortex breakdown. *J Fluid Mechanics*, 45, 1971.

[14] F D Sabatino, T F Guiberti, J P Moeck, W L Roberts, and D A Lacoste. Experimental Analysis of the Effect of Fuels on the Flame Describing Function of a Swirl-Stabilized Premixed Flame. *Proceedings of ASPACC*, (December):5–8, 2017.

[15] B Guo, Tim A. Langrish, G, and D F Fletcher. Simulation of Turbulent Swirl Flow in an Axisymmetric Sudden Expansion. *AIAA Journal*, 39(1):96–102, 2001.

[16] H. AbdelGayed and W. Abdelghaffar. Main flow characteristics in a lean premixed swirl stabilized gas turbine combustor Numerical computations. *American Journal of Scientific and Industrial Research*, 4(1):123–136, 2013.

[17] A V Medina and R March. CFD predictions of Swirl burner aerodynamics with variable outlet configurations. *Proceedings of the Global Conference on Energy and Sustainable Development*, pages 1–7, 2015.

[18] C O Umeh and Z Rusak. Swirling Flows in an Axisymmetric Lean Premixed Combustor. *36th AIAA Fluid Dynamics Conference and Exhibit*, (June):1–24, 2006.

[19] D Tokekar. Modeling and Simulation of Reacting Flows in Lean-Premixed Swirl-Stabilized Gas Turbine Comustor, 2008.

[20] H AbdelGayed and W Abdelghaffar. Main flow characteristics in a lean premixed swirl stabilized gas turbine combustor. *American Journal of Scientific and Industrial Research*, 4(1):123–136, 2013.

[21] A T Abdallah, L E Eriksson, I R Sigfrid, and R Whiddon. Cfd Investigation of Swirl-Stabilized Flexi-Fuel Burner Using Methane-Air Mixture for Gas Turbines. *International Society for Airbreathing Engines, ISABE, Gothenburg, 2011*, pages 1–13, 2011.

[22] L Anetor, E Osakue, and C Odetunde. Reduced mechanism approach of modeling pre-mixed propane-air mixture using ansys fluent. *Engineering Journal*, 16(1):67–86, 2012.

[23] D Pampaloni, D Bertni, S Puggelli, L Mazzeii, and Andreini A. Methane swirl-stabilized lean burn flames assessment of scale resolving simulations. *Energy procedia*, 126:834–841, 2017.

[24] F Veiga. Numerical Simulation of a Lean Premixed Hydrogen Combustor for Aero Engines.

[25] J Li, S K Chou, W M Yang, and Z W Li. A numerical study on premixed micro-combustion of CH4-air mixture: Effects of combustor size, geometry and boundary conditions on flame temperature. *Chemical Engineering Journal*, 150(1):213–222, 2009.

[26] A Bahramian, M Maleki, and B Medi. CFD modeling of flame structures in a gas turbine combustion reactor: Velocity, temperature, and species distribution. *International Journal of Chemical Reactor Engineering*, 15(4), 2017.

[27] H Bao. Development and Validation of a New EddyDissipation Concept (EDC) Model for MILD Combustion. 2017.

[28] J A V OIJEN and L P H D GOEY. Modelling of Premixed Laminar Flames using Flamelet-Generated Manifolds. *Combustion Science and Technology*, 161(1):113–137, 2000.

[29] S Ouali, A Bentebbiche, and T Belmrabet. Numerical simulation of methane-air equivalence ratio effect on premixed low swirl stabilized flame. *Journal of the Brazilian Society of Mechanical Sciences and Engineering*, 37(2):747–760, 2015.

[30] W J S Ramaekers, B A Albrecht, J A Van Oijen, L P H de Goey, and R G L M Eggels. The application of Flamelet Generated Manifolds in modelling of turbulent partially-premixed flames. *Proceedings of the Fluent Benelux User Group Meeting, (pp. 3D). Belgium, Château de Limelette*, pages 1–16, November 2014.

[31] S Kedukodi. Numerical Analysis of Flow and Heat Transfer through a Lean Premixed Swirl Stabilized Combustor Nozzle. 2017.

[32] P Nakod, R Yadav, P Rajeshirke, and S Orsino. A Comparative Computational Fluid Dynamics Study on Flamelet-Generated Manifold and Steady Laminar Flamelet Mod-

eling for Turbulent Flames. *Journal of Engineering for Gas Turbines and Power*, 136(8):081504, 2014.

[33] N Shelil, P Said, A J Griffiths, N Syred, and P Said. Numerical Study of Stability Limits of Premixed-Swirl Flames. (August):1–15, 2009.

[34] M Tidswell and S Muppala. A numerical study of turbulent flame speed models for H 2 /CH 4 /Air premixed combustion. *International Journal of Enhanced Research in Science Technology & Engineering*, 3(6):407–422, 2014.

[35] M D Hipp. RANS simulation of methane combustion in a LowSwirl Burner, 2010.

[36] W Polifke, P Flohr, and M Brandt. Modeling of Inhomogeneously Premixed Combustion With an Extended TFC Model. *Journal of Engineering for Gas Turbines and Power*, 124(1):58, 2002.

[37] S Park, S Gadhiraju, J Pandit, S Ekkad, F Liberatore, Y H Ho, and R Srinivasan. Effects of reacting conditions on flow fields in a swirl stabilized lean premixed can combustor. *ASME*, 2018.

[38] T O'Doherty O, Lucca-Negro. Vortex breakdown: a review. *Progress in Energy and Combustion Science*, pages 431–481, 2001.

[39] S Leibovich. The structure of vortex breakdown. *Annu Rev Fluid Mech*, 10:221–246, 1978.

[40] J K. Harvey. Some observations of the vortex breakdown phenomenon. *J Fluid Mechanics*, 14:585–592, 1962.

[41] J H Faler and S Leibovich. Disrupted states of vortex flow and vortex breakdown. *Phys Fluids*, 20:1385–1400, 1977.

[42] Shelil, N. Flashback Studies with Premixed Swirl Combustion. pages 1–227, 2009.

[43] K Takeo and T Kunihiko. *Computational Fluid Dynamics: Incompressible Turbulent Flows*. Sringer, Cham.

[44] ANSYS Inc. Ansys fluent theory guide, 2012.

[45] Li S, Zhongguang S, Yazhou S, Ruixin W, and Hui Z. LES of Swirl Angle on Combustion Dynamic and NOx Formation in a Hybrid Industrial Combustor. *International Journal of Heat and Technology*, 34(2):197–206, 2016.

[46] V L Zimont and A N Lipatnikov. A numerical model of premixed turbulent combustion of gases. *Chem. Phys. Reports*, 14(7):993–1025, 1995.

[47] V L Zimont, W Polifke, M Bettelini, and W Weisenstein. An Efficient Computational Model for Premixed Turbulent Combustion at High Reynolds Numbers Based on a Turbulent Flame Speed Closure. *ASME. J. Eng. Gas Turbines Power*, 120(3):526–532, 1998.

[48] Poinsot and Veynante. *Theoretical and Numerical Combustion*. McGraw-Hill, New York.

[49] B F Magnussen and B H Hjertager. On mathematical modeling of turbulent combustion with special emphasis on soot formation and combustion. *Symposium (International) on Combustion*, 16(1):719–729, 1977.

[50] D A Lacoste, J P Moeck, D Durox, C O Laux, and T Schuller. Effect of Nanosecond Repetitively Pulsed Discharges on the Dynamics of a Swirl-Stabilized Lean Premixed Flame. *Journal of Engineering for Gas Turbines and Power*, 135(10):101501, 2013.

[51] Ohio Supercomputer Center. Ohio supercomputer center, 1987.

[52] G P Smith, D M Golden, M Frenklach, and N M Moriarty. Gri-mech 3.0, 2000. http://www.me.berkeley.edu/gri_mech/.

[53] Lapack's user guide, 1999.

[54] J M Beer and N A Chigier. *Combustion Aerodynamics*. Applied Sciences.

[55] D Ebi and N T Clemens. Experimental investigation of upstream flame propagation during boundary layer flashback of swirl flames. *MDPI*, 2016.

[56] A Nauert, P Petersson, M Linne, and A Dreizler. Experimental analysis of flashback in lean premixed swirling flames: conditions close to flashback. *Experiments in Fluids*, 43:89–100, 2007.

[57] D Nguyen and V Sebastian. Computational study of the laminar reaction front properties of diluted methanol air flames enriched by the fuel reforming product. *Engergy and Fuels*, 31:9991–10002, 2017.

[58] P A Strakey, D S Woodruff, T C Williams, and R W Schefer. Oh-planar fluorescence measurements of pressurized, hydrogenpremixed flames in the simval combustor. *AIAA*, 46, 2008.

[59] Q Li, W Jin, and Z Huang. Laminar flame characteristics of c1-c5 primary alcohol-isooctane blends at elevated temperature. *Combustion and Flame*, 168:39–52, 2016.